



**University of  
Zurich**<sup>UZH</sup>

**Zurich Open Repository and  
Archive**

University of Zurich  
University Library  
Strickhofstrasse 39  
CH-8057 Zurich  
[www.zora.uzh.ch](http://www.zora.uzh.ch)

---

Year: 2014

---

## **The formation of stellar nuclear discs in bar-induced gas inflows**

Cole, David R ; Debattista, Victor P ; Erwin, Peter ; Earp, Samuel W F ; Roškar, Rok

**Abstract:** The role of gas in the mass assembly at the nuclei of galaxies is still subject to some uncertainty. Stellar nuclear discs bridge the gap between the large-scale galaxy and the central massive objects that reside there. Using a high-resolution simulation of a galaxy forming out of gas cooling and settling into a disc, we study the formation and properties of nuclear discs. Gas, driven to the centre by a bar, settles into a rotating star-forming nuclear disc (ND). This ND is thinner, younger, kinematically cooler and more metal rich than the surrounding bar. The ND is elliptical and orthogonal to the bar. The complex kinematics in the region of the ND are a result of the superposition of older stars streaming along the bar and younger stars circulating within the ND. The signature of the ND is therefore subtle in the kinematics. Instead the ND stands out clearly in metallicity and age maps. We compare the model to the density and kinematics of real galaxies with NDs finding qualitative similarities. Our results suggest that gas dissipation is very important for forming nuclear structures

DOI: <https://doi.org/10.1093/mnras/stu1985>

Posted at the Zurich Open Repository and Archive, University of Zurich

ZORA URL: <https://doi.org/10.5167/uzh-154887>

Journal Article

Published Version

Originally published at:

Cole, David R; Debattista, Victor P; Erwin, Peter; Earp, Samuel W F; Roškar, Rok (2014). The formation of stellar nuclear discs in bar-induced gas inflows. *Monthly Notices of the Royal Astronomical Society*, 445(4):3352-3369.

DOI: <https://doi.org/10.1093/mnras/stu1985>

# The formation of stellar nuclear discs in bar-induced gas inflows

David R. Cole,<sup>1</sup>★ Victor P. Debattista,<sup>1</sup> Peter Erwin,<sup>2,3</sup> Samuel W. F. Earp<sup>1</sup>  
and Rok Roškar<sup>4</sup>

<sup>1</sup>Jeremiah Horrocks Institute, University of Central Lancashire, Preston PR1 2HE, UK

<sup>2</sup>Max-Planck-Institut für extraterrestrische Physik, Giessenbachstrasse, D-85748 Garching, Germany

<sup>3</sup>Universitäts-Sternwarte München, Scheinerstrasse 1, D-81679 München, Germany

<sup>4</sup>Institute for Computational Science, University of Zürich, Wintherturerstrasse 190, CH-8057 Zürich, Switzerland

Accepted 2014 September 22. Received 2014 September 19; in original form 2014 May 14

## ABSTRACT

The role of gas in the mass assembly at the nuclei of galaxies is still subject to some uncertainty. Stellar nuclear discs bridge the gap between the large-scale galaxy and the central massive objects that reside there. Using a high-resolution simulation of a galaxy forming out of gas cooling and settling into a disc, we study the formation and properties of nuclear discs. Gas, driven to the centre by a bar, settles into a rotating star-forming nuclear disc (ND). This ND is thinner, younger, kinematically cooler and more metal rich than the surrounding bar. The ND is elliptical and orthogonal to the bar. The complex kinematics in the region of the ND are a result of the superposition of older stars streaming along the bar and younger stars circulating within the ND. The signature of the ND is therefore subtle in the kinematics. Instead the ND stands out clearly in metallicity and age maps. We compare the model to the density and kinematics of real galaxies with NDs finding qualitative similarities. Our results suggest that gas dissipation is very important for forming nuclear structures.

**Key words:** galaxies: bulges – galaxies: evolution – galaxies: kinematics and dynamics – galaxies: nuclei – galaxies: structure.

## 1 INTRODUCTION

The central regions of galaxies host a wide variety of structures. On the largest scales, pseudo-bulges are thought to form from the secular evolution of discs (see the review of Kormendy & Kennicutt 2004). At the opposite extreme are supermassive black holes and nuclear star clusters. The growth of these is still a matter of debate. Nuclear star clusters show multiple populations (Schinnerer, Böker & Meier 2003; Rossa et al. 2006; Walcher et al. 2006; Seth et al. 2010; Lyubenova et al. 2013) often with episodes of star formation within the last 100 Myr, suggesting that gas is able to reach the centres of galaxies (Seth et al. 2006, 2008; Hartmann et al. 2011; De Lorenzi et al. 2013).

Disc-like structures (by their discy isophotes) are observed in the centres of galaxies at a wide range of scales. They are distinct in that they lie outside of the region where light from the main disc dominates. They are smaller than the bulge but often extending beyond the central nuclear star cluster (e.g. Balcells, Graham & Peletier 2007). [See Section 6 for examples of nuclear discs (NDs) in real galaxies.] NDs are found in spiral galaxies (Zasov & Moiseev 1999; Pizzella et al. 2002; Dumas et al. 2007; García-Burillo &

Combes 2012) and in 20 per cent of early-type galaxies (Scorza & van den Bosch 1998; Kormendy & Gebhardt 2001; de Zeeuw et al. 2002; Emsellem et al. 2004; Trujillo et al. 2004; Krajnović et al. 2008; Ledo et al. 2010). Krajnović et al. (2008) found NDs in early-type galaxies are associated with fast rotators. Near-infrared *Hubble Space Telescope* (HST) imaging has also provided indirect evidence for NDs as discy isophotes in the nuclei of early-type galaxies (Ravindranath et al. 2001) or photometrically distinct exponential components in bulges (Balcells et al. 2003). Erwin et al. (2014) also found evidence for NDs which they call ‘discy pseudo-bulges’.

Understanding the formation of NDs is very important for a clearer picture of the assembly of mass at the centres of galaxies. The formation of NDs is generally thought to require in situ star formation. A number of ideas about how gas can be funnelled to the central regions of galaxies have been proposed. Observations of luminous and ultraluminous infrared galaxies have found NDs in their nuclei. These have masses in the range  $10^8$ – $10^{10} M_\odot$ , effective radii of a few hundred parsecs and  $v/\sigma = 1$ –5 (Medling et al. 2014). Medling et al. (2014) conclude that mergers funnel gas to the centre of the galaxy prior to star formation. Likewise, simulations have predicted that NDs are able to form in gas-rich galaxy mergers (Mayer, Kazantzidis & Escala 2008; Mayer et al. 2010; Chapon, Mayer & Teyssier 2013). McDermid et al. (2006) found NDs and counter-rotating cores in the central kpc of early-type galaxies and

★ E-mail: dcole@uclan.ac.uk

evidence for recent circumnuclear star formation. The presence of dynamically decoupled features such as a counter-rotating disc in NGC 4458 (Morelli et al. 2004, 2010) and a disc rotating perpendicular to the main galactic disc (Bertola et al. 1999; Corsini et al. 1999, 2012; Pizzella et al. 2002) can be explained by the capture of external gas. However interactions may not be the main mechanisms driving gas to nuclei in more isolated galaxies, where observations show that there is continuing star formation in some NDs e.g. in NGC 5845 (Kormendy et al. 1994) and NGC 4486A (Kormendy et al. 2005) and their stellar populations have both young and old components (van den Bosch, Jaffe & van der Marel 1998; Krajnović & Jaffe 2004; Morelli et al. 2004; Corsini et al. 2012). Mechanisms that have been proposed for driving gas to small radii in such systems include nested bars (Shlosman, Frank & Begelman 1989), the magnetorotational instability (Milosavljević 2004) and cloud–cloud mergers (Bekki 2007). Agarwal & Milosavljević (2011) proposed that NDs can form out of the debris of infalling star clusters and Portinari et al. (2013) showed that the available photometric and kinematic data are still consistent with this idea. However, detailed modelling (De Lorenzi et al. 2013) and comparison to simulations (Hartmann et al. 2011) of the kinematics of the nuclear star cluster in NGC 4244 (Seth et al. 2008) reveal that gas dissipation had to have played a major role in the formation of its nuclear cluster, indicating that some gas must be able to reach the inner  $\sim 10$  pc.

Possibly associated with NDs are  $\sigma$ -drops which are galaxies having a significant drop in velocity dispersion at the nucleus (see e.g. Emsellem et al. 2001). One explanation for these  $\sigma$ -drops is that there is an inflow of gas to the nuclear region which creates a dynamically cool disc where stars form, reducing the central velocity dispersion (Wozniak et al. 2003; Comerón, Knapen & Beckman 2008). In face-on galaxies, Méndez-Abreu (2014) imaged small NDs cospatial with the region of the  $\sigma$ -drops.

Bars are thought to be a mechanism for driving gas to small radii. Falcón-Barroso et al. (2004) found that this was a natural explanation for the presence of a ND in the edge-on S0 galaxy NGC 7332, where the presence of a bar is inferred from a boxy/peanut shape (Seifert & Scorza 1996). Barred spiral galaxies have more molecular gas in their central kiloparsec than unbarred galaxies (Sakamoto et al. 1999; Sheth et al. 2005). Wang et al. (2012) examined a sample of over 3700 face-on disc galaxies and found that there is a correlation between the presence of strong bars and centrally enhanced star formation. They also found that the increase in star formation depends primarily on the ellipticity of the bar and not on the size of the bar or on the mass and structure of the host galaxy. Dumas et al. (2007), studying active and non-active galaxies, found that NDs are associated with enhanced active galactic nucleus (AGN) activity. Hao et al. (2009) found that the bar fraction was higher in galaxies hosting an AGN and in star-forming galaxies than in inactive galaxies. Hicks et al. (2013) showed that Seyfert galaxies have a more centrally concentrated nuclear stellar and molecular gas surface brightness profile probably due to a ND-like structure composed of gas and stars in a region out to 250 pc.

Here we study the morphology and evolution of a simulation of a disc galaxy using smooth particle hydrodynamics (SPH) at high resolution. The model of this galaxy developed in isolation and so the resulting features are purely due to internal origin. We concentrate on the central region of the model. Section 2 describes the simulation methods. Section 3 presents the global morphology and star formation history of the model. Section 4 focuses on the properties of the nuclear stellar disc, while Section 5 discusses the properties of the gas in the nuclear region. Section 6 compares our

model to several early-type galaxies. Finally, Section 7 presents our conclusions.

## 2 THE SIMULATION

The simulation we consider here is the same as model HG1 of Gardner et al. (2014) and the model studied by Ness et al. (2014). The model has a disc galaxy forming inside a corona of pressure-supported gas embedded in a dark matter halo, a technique we have used extensively for studying disc galaxy evolution (Roškar et al. 2008, 2012). The main computational difference here with respect to that work is that we have employed higher mass resolution, which allows a higher star formation threshold and an increased supernova feedback coupling. The dark matter halo consists of  $5 \times 10^6$  dark matter particles in two mass species:  $4.5 \times 10^6$  particles of mass  $m_p = 8.5 \times 10^4 M_\odot$  while the remainder have a mass of  $1.7 \times 10^6 M_\odot$ . The dark matter particles are arranged in two mass shells, with particles initially inside 56 kpc having the low mass and those outside having the larger mass. This arrangement allows us to increase resolution inside 56 kpc. These particles all have a force softening of  $\epsilon = 103$  pc. The halo has virial radius  $r_{200} = 198$  kpc, concentration  $c = 19$  and virial mass  $M_{200} = 9.0 \times 10^{11} M_\odot$ . Mixed in with the dark matter is a hot gas corona, consisting of  $5 \times 10^6$  particles, initially in pressure equilibrium. Gas particles have  $\epsilon = 50$  pc and, initially, all have equal mass  $2.7 \times 10^4 M_\odot$ . The corona has the same density profile normalized to a total mass 11 per cent that of the dark halo. We give the gas angular momentum with  $L_z \propto R$  such that  $\lambda \approx 0.041$ . No stellar particles are present at the start of the simulation since all stars form out of gas that cools and reaches a density high enough to trigger star formation.

The simulation was evolved with the *N*-body+SPH code GASOLINE (Wadsley, Stadel & Quinn 2004). We use a base time step of 10 Myr with a refinement parameter  $\eta = 0.175$ , and an opening angle of  $\theta = 0.7$ . The time step of gas particles also satisfies the condition  $\delta t_{\text{gas}} = \eta_{\text{courant}} h / [(1 + \alpha)c + \beta \mu_{\text{max}}]$ , where  $\eta_{\text{courant}} = 0.4$ ,  $h$  is the SPH smoothing length,  $\alpha$  is the shear coefficient, which is set to 1,  $\beta = 2$  is the viscosity coefficient and  $\mu_{\text{max}}$  is described in Wadsley et al. (2004).  $\eta_{\text{courant}}$  is the refinement parameter for SPH particles and controls their time step size. The SPH kernel is defined using the 32 nearest neighbours. Gas cooling is calculated without taking into account the gas metallicity.

We use the gas cooling, star formation and stellar feedback prescriptions of Stinson et al. (2006). A gas particle undergoes star formation if it has number density  $n > 100 \text{ cm}^{-3}$ , temperature  $T < 15\,000$  K and is part of a converging flow; efficiency of star formation is 0.1, i.e. 10 per cent of gas eligible to form stars spawn stars per dynamical time. Star particles form with an initial mass of 35 per cent that of the gas particle, which at our resolution corresponds to  $9.4 \times 10^3 M_\odot$ . Gas particles can spawn multiple star particles but once they drop below 21 per cent of their initial mass the remaining mass is distributed amongst the nearest neighbours, leading to a decreasing number of gas particles. Each star particle represents an entire stellar population with a Miller–Scalo (Miller & Scalo 1979) initial mass function. The evolution of star particles includes feedback from Type II and Type Ia supernovae (SNeII, SNeIa), with their energy injected into the interstellar medium (ISM). The effect of the supernovae explosions is modelled at the subgrid level as a blast wave propagating through the ISM (Stinson et al. 2006). As in Governato et al. (2010), we assume that  $0.4 \times 10^{51}$  erg of energy per supernova couple to the ISM. We also include feedback from asymptotic giant branch (AGB) stellar winds. The gas corona has zero metallicity to start with; we track

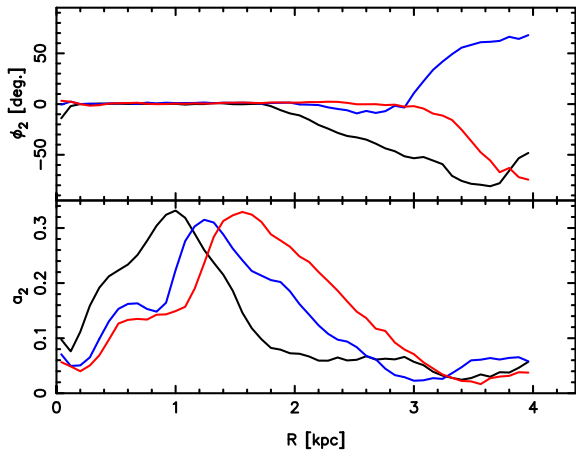


**Figure 1.** The  $m = 2$  Fourier amplitude,  $a_2$  (bottom), and relative phase,  $\phi_2$  (top), of the stellar density distribution at 6 (black lines), 8 (blue lines) and 10 Gyr (red lines).

the production of iron and oxygen in the simulation using the yields of Woosley & Weaver (1995). Diffusion of metals (e.g. Loebman et al. 2011) between gas particles was not used in this simulation. We also do not include any feedback from an AGN since the model does not contain a supermassive black hole.

### 3 GLOBAL PROPERTIES OF THE MODEL

By the end of the simulation, at  $\sim 10$  Gyr, the stellar disc consists of  $\sim 1.1 \times 10^7$  particles. The total stellar mass of the galaxy is  $\sim 6.5 \times 10^{10} M_\odot$ , typical of an  $L_*$  galaxy such as the Milky Way. It is not, however, an exact analogue of the Milky Way as the scale length of the disc is smaller, at  $R_d \simeq 1.7$  kpc, whereas the Milky Way has  $1.8 \leq R_d \leq 4.0$  kpc (e.g. Ojha 2001; Chang, Ko & Peng 2011; McMillan 2011). As shown in Gardner et al. (2014), the bar forms a clear box/peanut shape as seen from the side, and an X-shape along the line of sight when observed like the Milky Way. Ness et al. (2014) showed further that the bulge stars have a range of ages, as observed in the Milky Way (Bensby et al. 2011, 2013; Valenti et al. 2013).

The amplitude  $a_2$  and relative phase  $\phi_2$  of the  $m = 2$  Fourier component are shown in Fig. 1. The peak of  $a_2$ , and the location where  $\phi_2$  deviates from a constant, increase with time, indicating that the bar is growing longer. By 10 Gyr the bar is  $\sim 3$  kpc long, increasing from  $\sim 2$  kpc at 6 Gyr. The evolution of the bar strength, defined as the amplitude of the global  $m = 2$  Fourier moment (e.g. Debattista & Sellwood 2000), is shown in Fig. 2. The bar forms at  $t \sim 3.2$  Gyr; its strength starts to grow at 5.2 Gyr and peaks at 5.8 Gyr and again at 6.5 Gyr.

Fig. 3 shows the global star formation history as well as that inside a number of radii. The global star formation rate is initially high, dropping rapidly to  $\sim 3 M_\odot \text{ yr}^{-1}$ . It does not show any maxima, in contrast to the region inside 500 pc, which has an episode of enhanced star formation at  $\sim 6$  Gyr.

### 4 NUCLEAR STELLAR DISC

Fig. 3 showed that the central 500 pc experiences increased star formation activity around  $\sim 6$  Gyr, compared with the rest of the simulation. We now turn our attention to the young stars within this central region. Fig. 4 shows the surface density of stars younger than 2 Gyr at 6, 8 and 10 Gyr. At 10 Gyr an elliptical, thin disc of

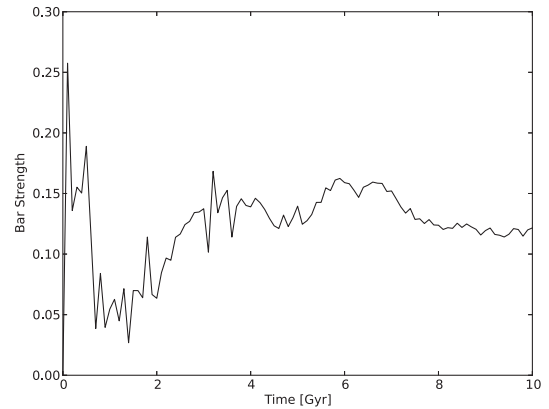


**Figure 2.** Evolution of the bar strength, defined as the amplitude of the  $m = 2$  Fourier moment.

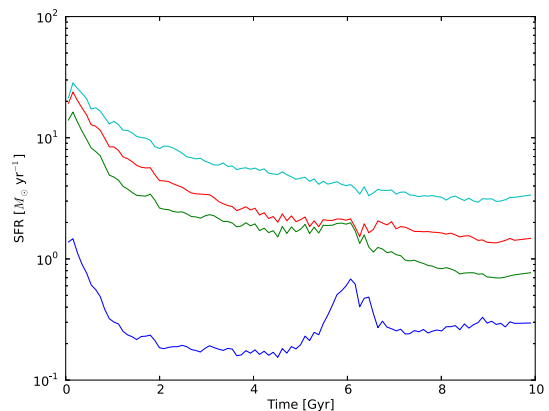


**Figure 3.** Star formation history of the model. The cyan line is the global history, the red, green and blue lines are the star formation histories inside 1 kpc, 500 and 100 pc, respectively. Note the peaks at  $\sim 6$  Gyr for the inner two regions.

stars is present inside  $\sim 1.5$  kpc. The ND is perpendicular to the main bar, which is horizontal<sup>1</sup> in Fig. 4 and is therefore most likely supported by the  $\times 2$  family of bar orbits, which is elongated in this way (Skokos, Patsis & Athanassoula 2002). [The  $\times 3$  orbits, which are also elongated perpendicular to the bar, are generally unstable (e.g. Sellwood & Wilkinson 1993) and very unlikely to be populated.] The ND can also be seen at 8 Gyr, but not at 6 Gyr. At 10 Gyr the ND is bounded by a nuclear ring which is part of the ND. There is a second nuclear ring at semimajor axis of  $\sim 300$  pc which is not very well resolved on its minor axis. These nuclear rings can be seen in the figures comparing our simulation to real galaxies in Section 6.

A lower limit on the mass of the ND at 10 Gyr is derived by considering the mass of stars younger than 3 Gyr enclosed within 1.5 kpc. This mass is  $5.5 \times 10^9 M_\odot$ . The bottom panel of Fig. 5 plots the azimuthally averaged surface density profile of stars. The profile is well approximated by an exponential with scale length 220 pc at 8 Gyr, increasing to 250 pc at 10 Gyr. The corresponding ND mass is  $2.5 \times 10^{10} M_\odot$  at 8 Gyr and  $3.1 \times 10^{10} M_\odot$  at 10 Gyr. For later comparison, we have also measured the density profiles for slits along the line-of-nodes for the system orientated

<sup>1</sup> In this paper we always show the system with the disc in the  $(x, y)$  plane and the bar rotated into the  $x$ -axis, except where noted.



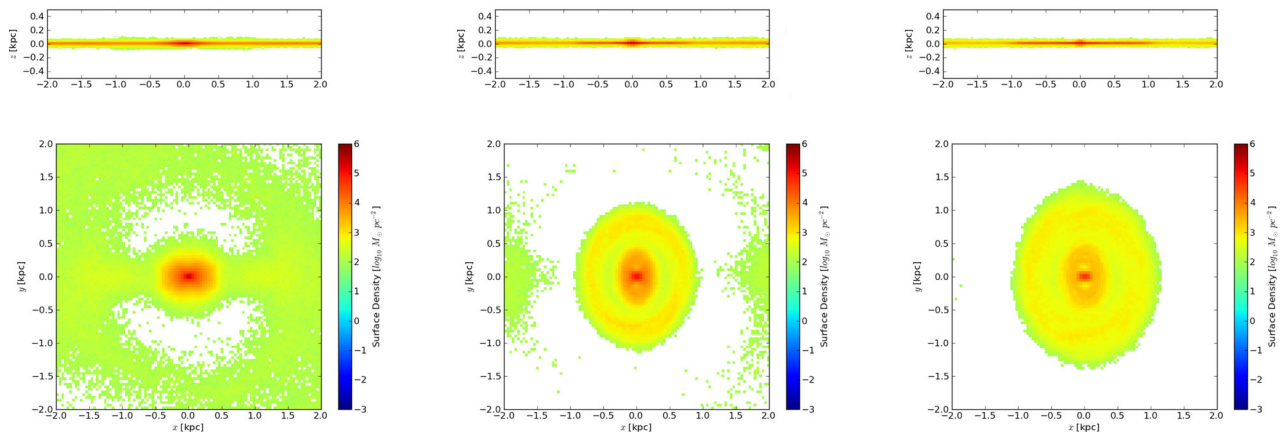


**Figure 4.** Face-on (bottom) and edge-on (top) surface density for the stars younger than 2 Gyr at 6 (left), 8 (centre) and 10 Gyr (right). The bar is along the  $x$ -axis in all panels.

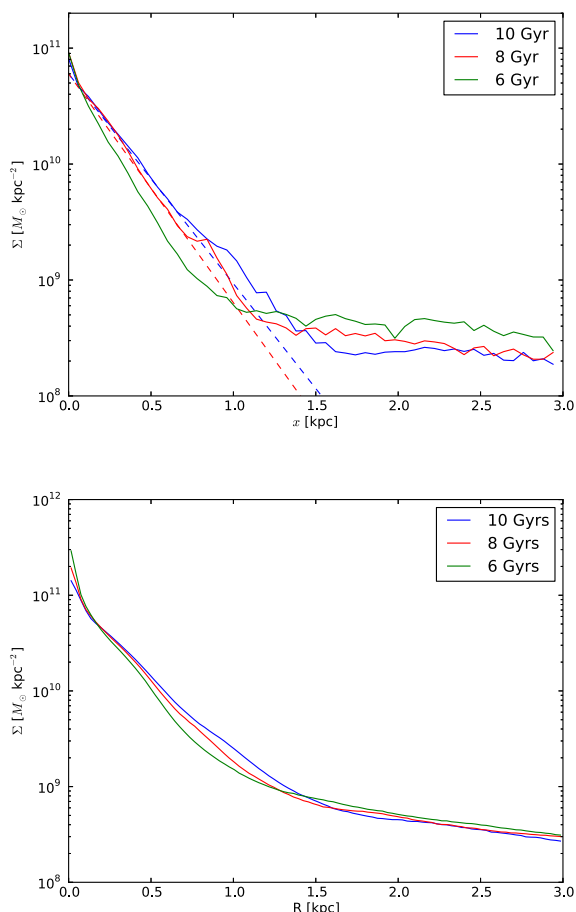


**Figure 5.** Stellar surface density profiles of the central regions at 6, 8 and 10 Gyr as indicated. Top: surface densities along the major axis of the ND with our model inclined at  $55^\circ$  the same as NGC 3945. The dashed lines indicate exponential profiles. Bottom: azimuthally averaged surface density profiles for the face-on orientation.

the same way as NGC 3945 (see Section 6.1.2 comparing our model to NGC 3945); these profiles are shown in the top panel of Fig. 5. Doing this we obtain a mass of  $1.6 \times 10^{10} M_\odot$  at 8 Gyr and  $1.9 \times 10^{10} M_\odot$  at 10 Gyr, the latter number corresponding to 29 per cent of the stellar mass of the model.

#### 4.1 Kinematics

We adopt cylindrical coordinates  $(R, \phi, z)$  to study the stellar kinematics. The left-hand column of Fig. 6 shows the mass-weighted average radial velocity,  $v_R$ , at 6, 8 and 10 Gyr. At all three times there are two diametrically opposed quadrants where  $v_R$  is negative (inward motion) and two where  $v_R$  is positive (outward motion). These radial motions of  $\sim 50 \text{ km s}^{-1}$  are indicative of non-circular motion in this inner region. While qualitatively similar, these maps exhibit a twisting of the ridge of peak  $|v_R|$  towards the major axis of the bar with time. For instance, the peak  $|v_R|$  in the first quadrant is at  $\sim 45^\circ$  to the bar at 6 Gyr slowly decreasing to  $\sim 25^\circ$  by 10 Gyr. At larger radii, beyond the ND ( $\gtrsim 1 \text{ kpc}$ ), the ridge of peak  $|v_R|$  twists away from the bar's major axis. This evolution can be understood by considering separately the motion of the old and young stars, as we do in Fig. 7. The ridge of peak  $|v_R|$  for the old ( $> 6 \text{ Gyr}$ ) stars is quite similar to that at 6 Gyr. For the young stars ( $< 3 \text{ Gyr}$ ), however, the peak  $v_R$  is both larger and rotated by  $\sim 90^\circ$  relative to the old stars. The radial motions at larger radii are caused by stars moving along the length of the bar, such that the negative  $v_R$  is on the leading side of the bar and the positive  $v_R$  is on the trailing side of the bar. The combination of these two independent motions leads to the twist of the ridge of peak  $|v_R|$  in the total population. The bottom left-hand panel of Fig. 7 also shows clearly the difference between the motions of stars in the ND and those in the bar, with  $v_R$  changing direction abruptly just outside the ND.

The right-hand column of Fig. 6 shows the mass-weighted average tangential velocity,  $v_\phi$ . At 6 Gyr the contours of  $v_\phi$  are parallel to the bar. After the ND forms, strong  $v_\phi$  peaks are located on the minor axis of the bar, i.e. along the major axis of the ND. Between 8 and 10 Gyr the peak  $v_\phi$  on the major axis of the ND also increases. The motions of the young stars, shown in Fig. 7, show the largest  $v_\phi$  is on the minor axis of the ND. The combination of the velocities from the main bar and the ND, however, leads to the strongest  $v_\phi$  on the ND's major axis while masking the ND kinematics on the bar's major axis.

The left-hand column of Fig. 8 shows the radial velocity dispersion,  $\sigma_R$ , while the right-hand column shows the vertical velocity dispersion,  $\sigma_z$ . After the ND forms both  $\sigma_R$  and  $\sigma_z$  along the major axis of the ND decline. This cooling occurs in an absolute sense, not just relative to the surrounding hotter bar. The decline in  $\sigma_z$  reflects that the new stars are forming in a thin population.

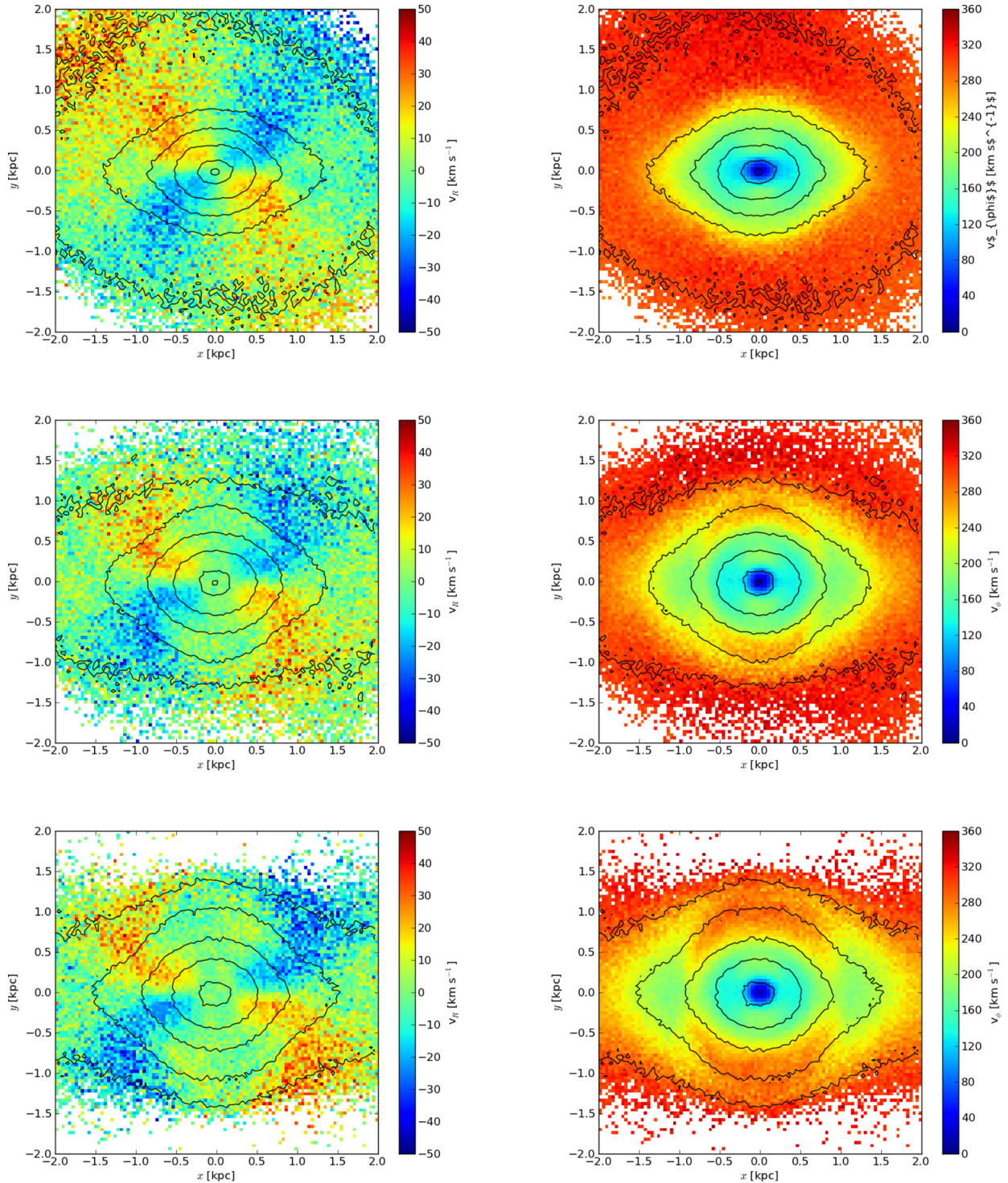


**Figure 6.** Mean stellar velocities at 6 (top row), 8 (middle row) and 10 Gyr (bottom row).  $v_R$  is shown in the left-hand column, while  $v_\phi$  is in the right-hand column. Contours indicate the stellar surface density.

The left-hand column of Fig. 9 shows the face-on mass-weighted Gauss–Hermite moment  $h_4$ . At 6 Gyr  $h_4$  has contours elongated like the bar with a near zero value at the centre increasing outwards. With the formation of the ND  $h_4$  increases. A strong peak forms on the ND major axis while minima are present on the bar’s major axis. By 10 Gyr the peak on the ND’s major axis strengthens further and the minima in the centre and along the bar’s major axis weaken. The

$h_4$  minimum on the bar’s major axis is a signature of the growing peanut shape of the bulge (Debattista et al. 2005; Méndez-Abreu et al. 2008).

Together,  $v_R$ ,  $v_\phi$ ,  $\sigma_R$ ,  $\sigma_z$  and  $h_4$  all indicate that a distinct, cool, thin ND, extending to  $R \sim 1.5$  kpc has formed by 10 Gyr. The ND is elliptical and elongated perpendicular to the main bar.



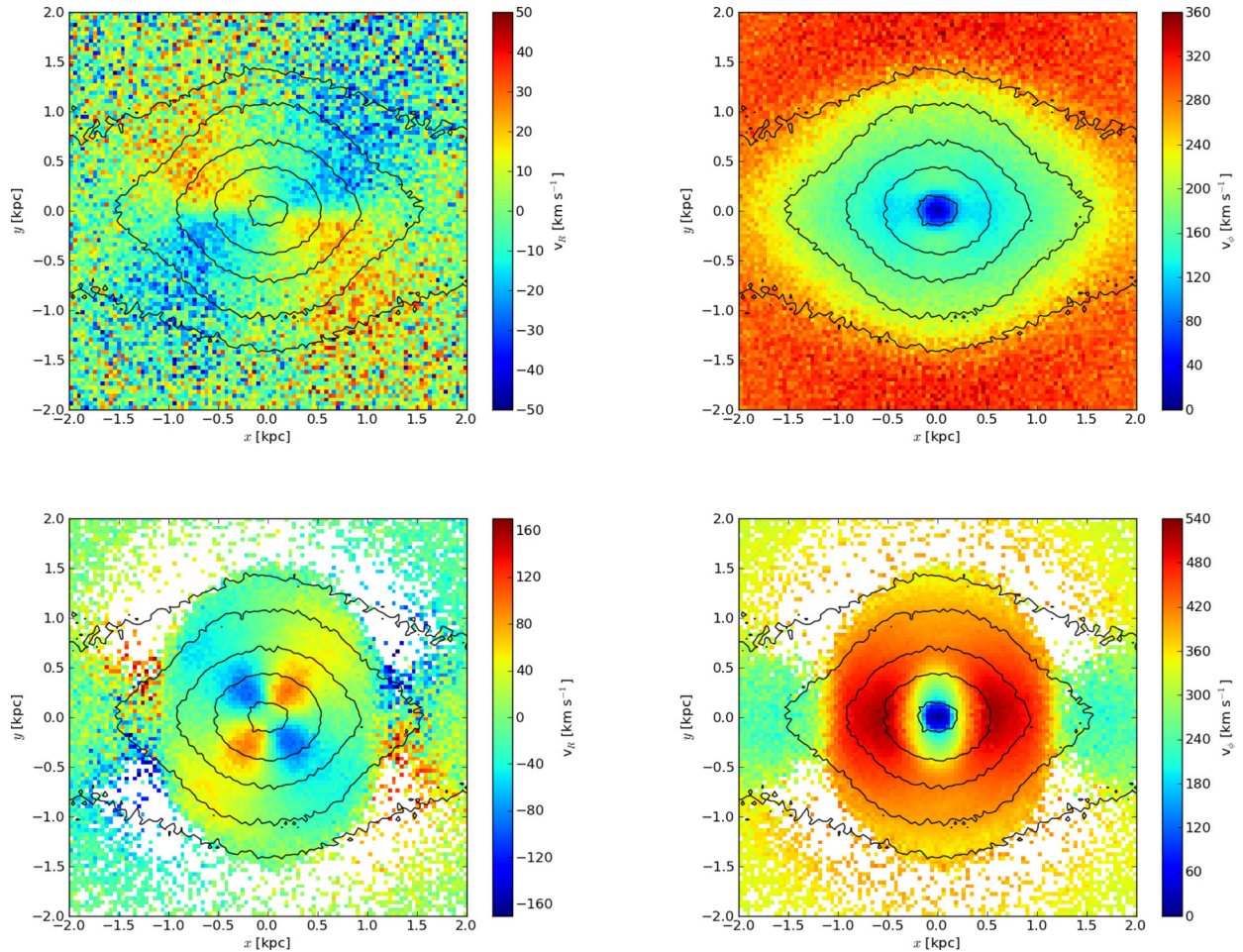


**Figure 7.** Mass-weighted mean stellar velocities at 10 Gyr broken down by age.  $v_R$  is shown in the left-hand column, while  $v_\phi$  is in the right-hand column. Stars older than 6 Gyr are shown in the top row while stars younger than 3 Gyr are shown in the bottom row. Note the different scales between the top and bottom rows. Contours indicate the total stellar surface density.

## 4.2 Ages

The right-hand column of Fig. 9 shows maps of the mass-weighted mean age of stars. Old stars are present in the central 1 kpc, which is dominated by the bar; further out the stellar populations are increasingly dominated by young stars formed in the ND. Perpendicular to the bar, a substantially younger population of stars is present at  $\sim 700$  pc, concentrated at the sides of the bar (see also Ness et al. 2014).

The distribution of stellar ages in barred galaxy simulations was studied by Wozniak (2007) and Wozniak & Michel-Dansac (2008, 2009). They used models with a pre-existing stellar disc, adding a gas disc with 10 per cent mass fraction, and evolved for 3 Gyr, at the end of which 46 per cent of the gas had been converted to stars. Wozniak (2007) found concentrations of young stars at the ends of the bar in their model. Our simulation also has young stars at the end of the bar, giving the mean age map a dimpled appearance along the bar’s major axis (see also Ness et al. 2014).

Wozniak (2007) and Wozniak & Michel-Dansac (2008) did not report a ND in their model (see figs 1 and 2 in Wozniak 2007), but did find a young population in a thin disc corresponding to 17 per cent of the stars in the inner 1 kpc. However, Wozniak & Michel-Dansac (2009) found a ND within a radius of 0.5 kpc. They conclude that their ND is associated with a  $\sigma$ -drop (see also Wozniak et al. 2003).

## 4.3 Chemistry

Fig. 10 shows mass-weighted maps of the mean stellar metallicity [Fe/H] and abundance [O/Fe]. The ND stands out very clearly in the metallicity maps as a region that is more metal rich than the bar. As we show below the star formation in this region from metal-rich gas gives rise to this metallicity signature of the ND, along the minor axis of the bar. The [O/Fe] maps instead show little direct evidence of the ND. Before it forms, the inner 500 pc region is  $\alpha$ -deficient but the surrounding region out to  $\sim 1$  kpc is  $\alpha$ -enhanced along the bar minor axis. Once the ND forms, however, [O/Fe] drops by  $\sim 0.05$ – $0.1$  dex, and the ND [O/Fe] blends in smoothly with that of the main bar.

## 5 COOL GAS PROPERTIES

Fig. 11 presents the evolution of the azimuthally averaged cool gas (defined as gas that has cooled to below 50 000 K) density within 3 kpc. This shows an increase by a factor of a few inside 1 kpc after 6 Gyr; this gas provides the fuel from which the stellar ND forms. Outside the ND, the gas density remains similar between 6 and 10 Gyr. Fig. 12 maps the surface density of the cool gas. The distribution at 6 Gyr is clumpy with no evidence of a ND, while after 8 Gyr it is more regular, and forms a disc with spirals connecting up to the gas inflowing along the leading edges of the

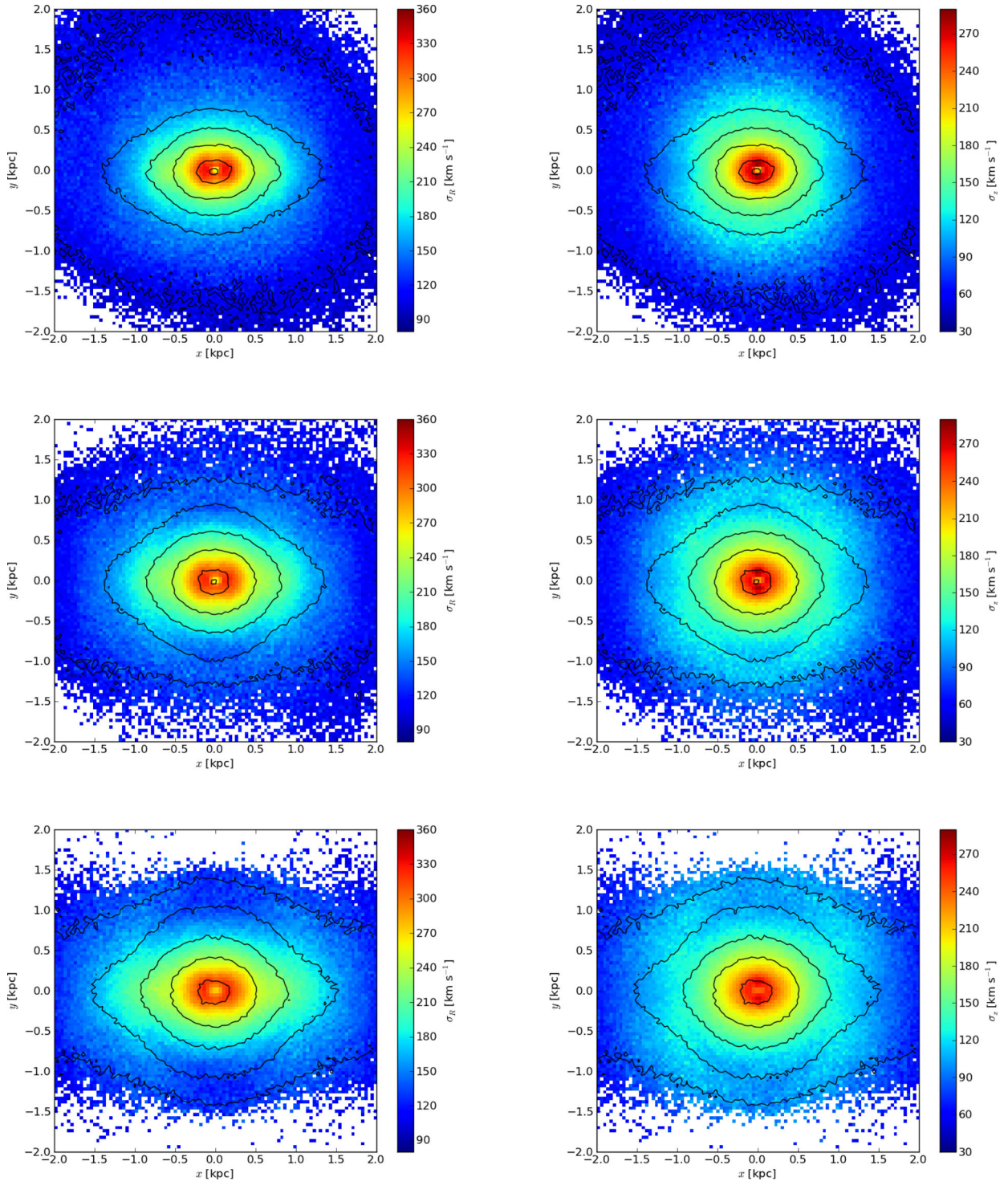


**Figure 8.** Mass-weighted stellar velocity dispersions at 6 (top row), 8 (middle row) and 10 Gyr (bottom row).  $\sigma_R$  is shown in the left-hand column, while  $\sigma_z$  is in the right-hand column. Contours indicate the stellar surface density.

bar. Fig. 2 showed that the bar grows stronger at about 6 Gyr, which is responsible for initiating the gas inflow into the nucleus. Except in the inner  $\sim 1$  kpc there is no evidence of enhanced star formation and no external perturbers are present in the simulation. The ND in this simulation therefore is seeded by the strengthening bar.

Fig. 13 shows the radial and tangential velocities of the cool gas. At 6 Gyr there is a gas inflow along the leading sides of the bar, arriving at the centre with peak inward (outward) velocity along the

bar's minor (major) axis. The tangential velocity is very disordered at 6 Gyr. This is a quite different velocity field from the stellar one at this time, and is dominated by dissipative inflows rather than by rotation. At 8 Gyr  $v_R$  has maxima and minima oriented at approximately  $45^\circ$  to the bar indicating the gas is now moving under the gravitational field of a massive ND. The peak radial velocities are progressively reduced over time but the inflow and outflow continues. The  $v_\phi$  maps show strong rotation in an elliptical disc



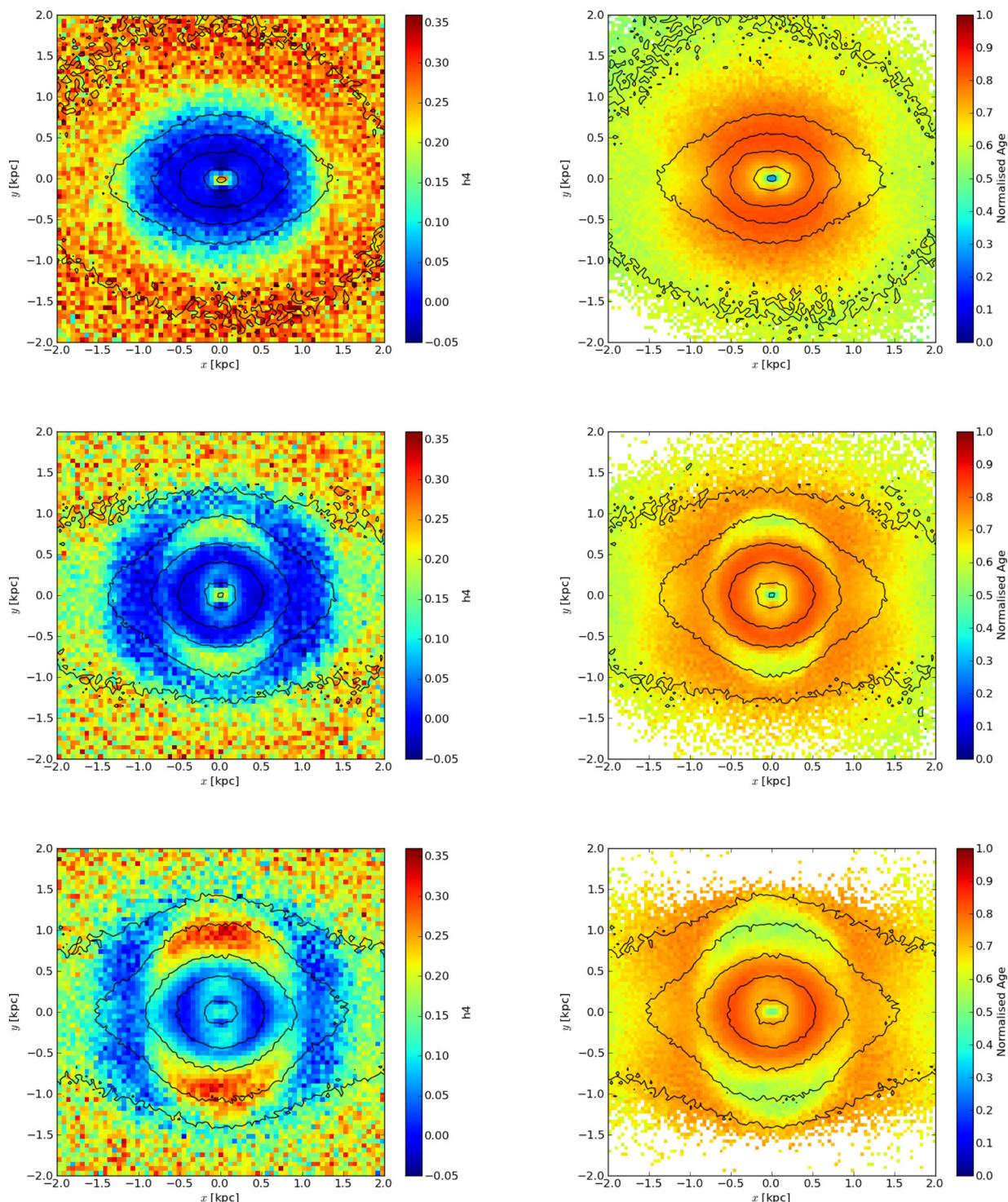


**Figure 9.** Left: face-on mass-weighted Gauss–Hermite vertical  $h_4$  kinematic moment. Right: mass-weighted mean stellar ages. To facilitate comparison of the different panels, the ages have been normalized by the time of each snapshot, i.e. the stellar ages are divided by the age of the simulation at the time of the snapshot: 6, 8 or 10 Gyr. The stellar surface density is indicated by the contours. The top, middle and bottom rows show 6, 8 and 10 Gyr.

at the later times. It is worth noting that  $v_R$  and  $v_\phi$  for the gas and the stars are rotated by  $\sim 90^\circ$  relative to each other (compare Figs 6 and 13). The cause of this is that the gas velocities reflect motions in the ND only, while the stellar velocities are a superposition of the motions of stars in the bar and in the ND. Instead the gas kinematics are quite similar to the kinematics of the young stars, as seen in Fig. 7.

Fig. 14 shows the mass-weighted nuclear gas chemistry. At 6 Gyr the gas has slightly elevated metallicity. The irregular distribution of both  $[\text{Fe}/\text{H}]$  and  $[\text{O}/\text{Fe}]$  is caused by gas inflowing from larger radii. Once the ND forms the cool gas is significantly more metal rich than the surrounding gas. At 8 Gyr the gas is  $\alpha$ -enhanced, a result of the rapid star formation already ongoing at 6 Gyr (see Fig. 3), although it is only later that the star formation settles into an ordered ND. By



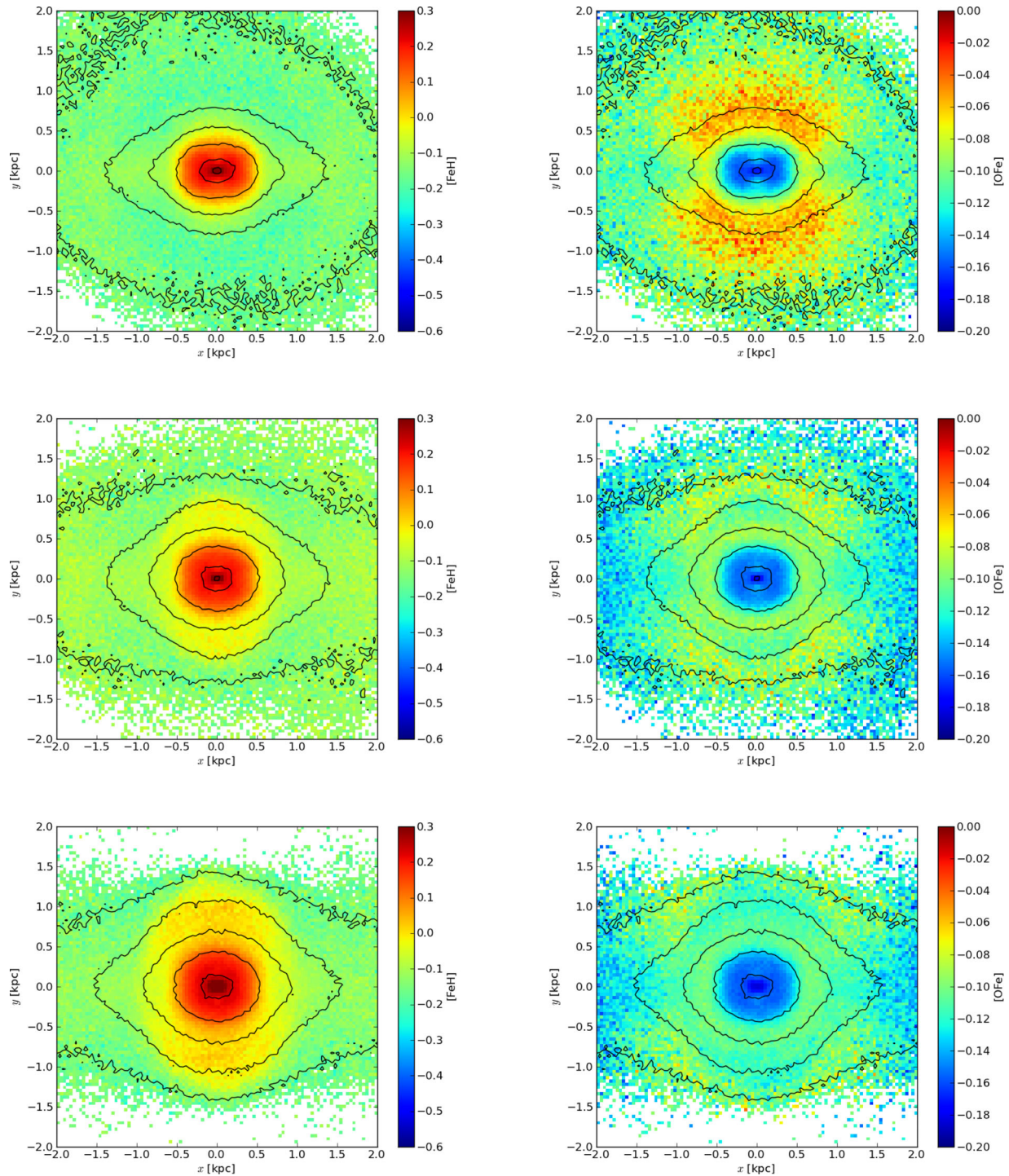


**Figure 10.** Mass-weighted mean stellar chemistry. The left-hand column shows  $[\text{Fe}/\text{H}]$ , while the right-hand column shows  $[\text{O}/\text{Fe}]$ . The top row is at 6 Gyr, the middle row is at 8 Gyr and the bottom row is at 10 Gyr. The stellar surface density is indicated by the contours.

10 Gyr the  $[\text{O}/\text{Fe}]$  of the gas has dropped to background levels as star formation continues to pollute the gas with SNIa ejecta.

## 6 COMPARISON TO REAL GALAXIES

### 6.1 Photometric comparisons

In this section we compare the simulation to three early-type disc galaxies where previous study has shown the existence of distinct,

moderately large NDs and/or massive stellar nuclear rings (which could plausibly be the most visible signature of an extended ND) inside bars (Erwin & Sparke 1999; Erwin et al. 2003; Erwin 2004; Comerón et al. 2010; Nowak et al. 2010). Further details concerning the NDs, including their relation to the central bulges, can be found in Erwin et al. (2014). For each galaxy, we orient the simulation to match the galaxy as best as possible, first reproducing the (deprojected) position angle (PA) of the bar relative to the line of nodes and then inclining the simulation by the same angle as the galaxy.

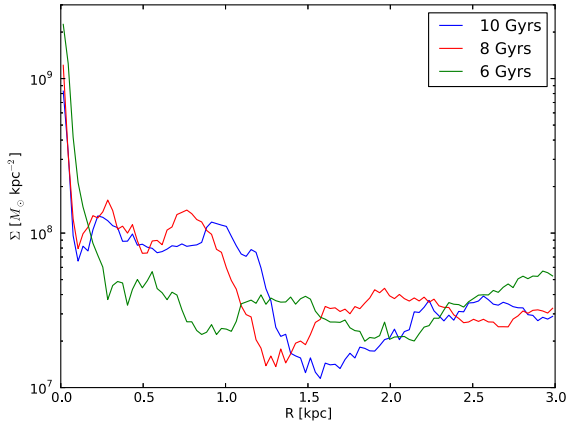


**Figure 11.** The azimuthally averaged cool gas surface density at 6, 8 and 10 Gyr as indicated.

### 6.1.1 Comparison to NGC 4371

NGC 4371 is a strongly barred S0 galaxy in the Virgo Cluster with a surface brightness fluctuation distance of 16.9 Mpc (Blakeslee et al. 2009). High-resolution imaging studies have shown that the interior of the bar is dominated by a very elliptical stellar nuclear ring with a radius of  $\approx 10.5$  arcsec (860 pc); there is little evidence for dust except in the very innermost ( $r < 1$  arcsec) regions and no evidence for current star formation, though the stellar nuclear ring is somewhat blue (Erwin & Sparke 1999; Comerón et al. 2010). The bar is aligned almost along the minor axis of the projected disc; the outer isophotes have an ellipticity of  $\approx 0.45$ , indicating an inclination of  $i \approx 58^\circ$  (assuming the disc has an intrinsic thickness of  $c/a = 0.2$ , typical for S0 galaxies; Lambas, Maddox & Loveday 1992; Padilla & Strauss 2008; Rodríguez & Padilla 2013). For the isophotes (upper right-hand panel of Fig. 15), we use an  $r$ -band image from the Isaac Newton Telescope (INT)/Wide Field Camera (WFC; Erwin, Pohlen & Beckman 2008); we also use an *HST* Advanced Camera for Surveys (ACS)/Wide Field Channel (WFC) *F850LP* image from the ACS Virgo Cluster Survey (Côté et al. 2004) for the ellipse fits (lower panels of the same figure).

The appearance of both the outer disc and the bar is very similar in the simulation and the real galaxy. A clear ellipticity peak *outside* the bar, at a semimajor axis  $a$  of 4.6 kpc in the simulation and 12 kpc in NGC 4371, is most likely due to a slightly non-circular outer ring; the ellipticity outside this peak approaches a roughly constant, lower value which is (in the case of the simulation) consistent with the adopted inclination. The bar itself manifests as a strong ellipticity minimum with a weak ellipticity peak in the centre of that minimum, accompanied by a strong twist in the PA.

Inside the bar, NGC 4371 has a strong inner ellipticity peak at around 800–900 pc, corresponding to the stellar nuclear ring. The simulation, in contrast, has two inner ellipticity peaks: the outer of the two corresponds to the outer nuclear ring, at the edge of the ND, while the inner peak is due to the inner nuclear ring. (The apparent inner ellipticity peak at  $a \sim 300$  pc in NGC 4371 is primarily a side effect of the combination of very elliptical isophotes from the nuclear ring and rounder isophotes from the bulge inside; see Erwin, Vega Beltrán & Beckman 2001.)

The fact that the ND in the simulation is slightly elliptical rather than circular results in a slight offset between the orientation of the outer disc ( $89^\circ$ ) and the ellipticity peaks due to the nuclear disc ( $\approx 91.5^\circ$ – $92^\circ$ ). A similar offset can be seen in NGC 4371 (PA =  $86^\circ$  for the outer disc and  $92^\circ$  for the inner ellipticity peak associated

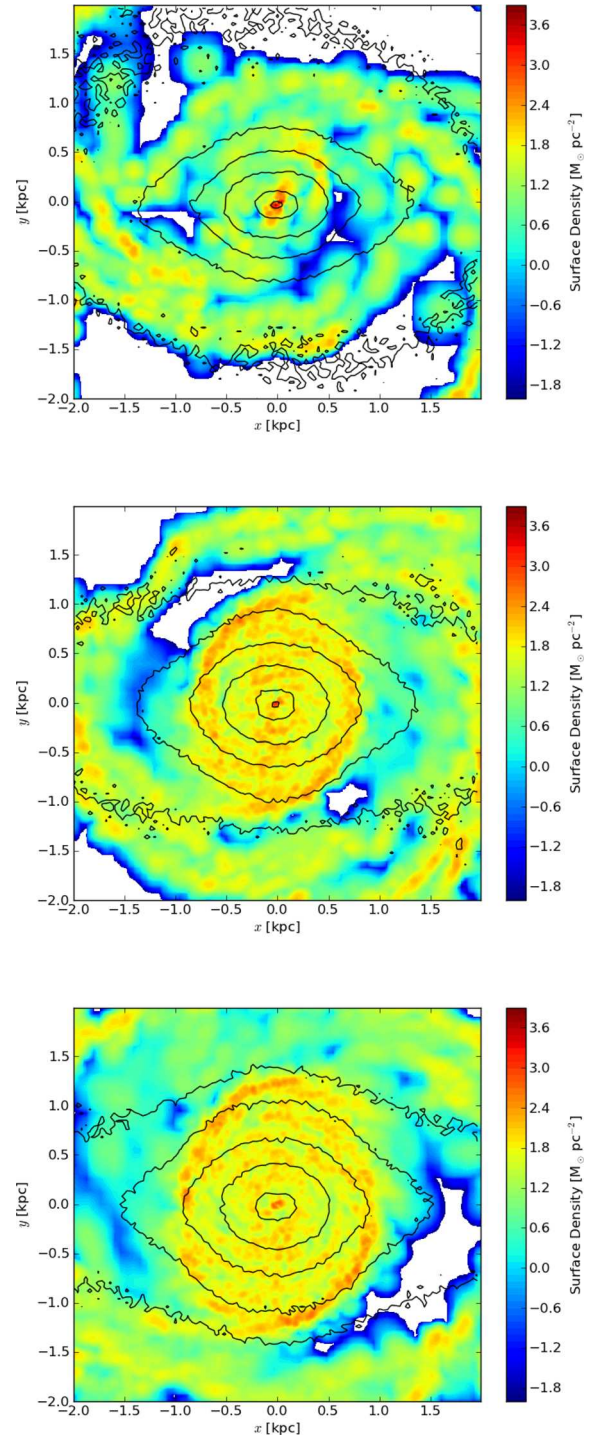


**Figure 12.** The cool gas surface density. The top row is at 6 Gyr, the middle row is at 8 Gyr and the bottom row is at 10 Gyr. The stellar surface density is indicated by the contours.

with the nuclear ring), which suggests that the nuclear disc/ring in NGC 4371 is slightly elliptical as well.

Erwin et al. (2014) estimate a ND mass of  $7.6 \times 10^9 M_\odot$  for NGC 4371, or 17 per cent of its total stellar mass, comparable to, but smaller than, the mass fraction measured in the model at 10 Gyr. The size of the ND, as a fraction of the deprojected radius at which the bar ellipticity peaks, is 0.17. If instead we use a bar radius at which the  $m = 2$  phase deviates from a constant by more than  $10^\circ$



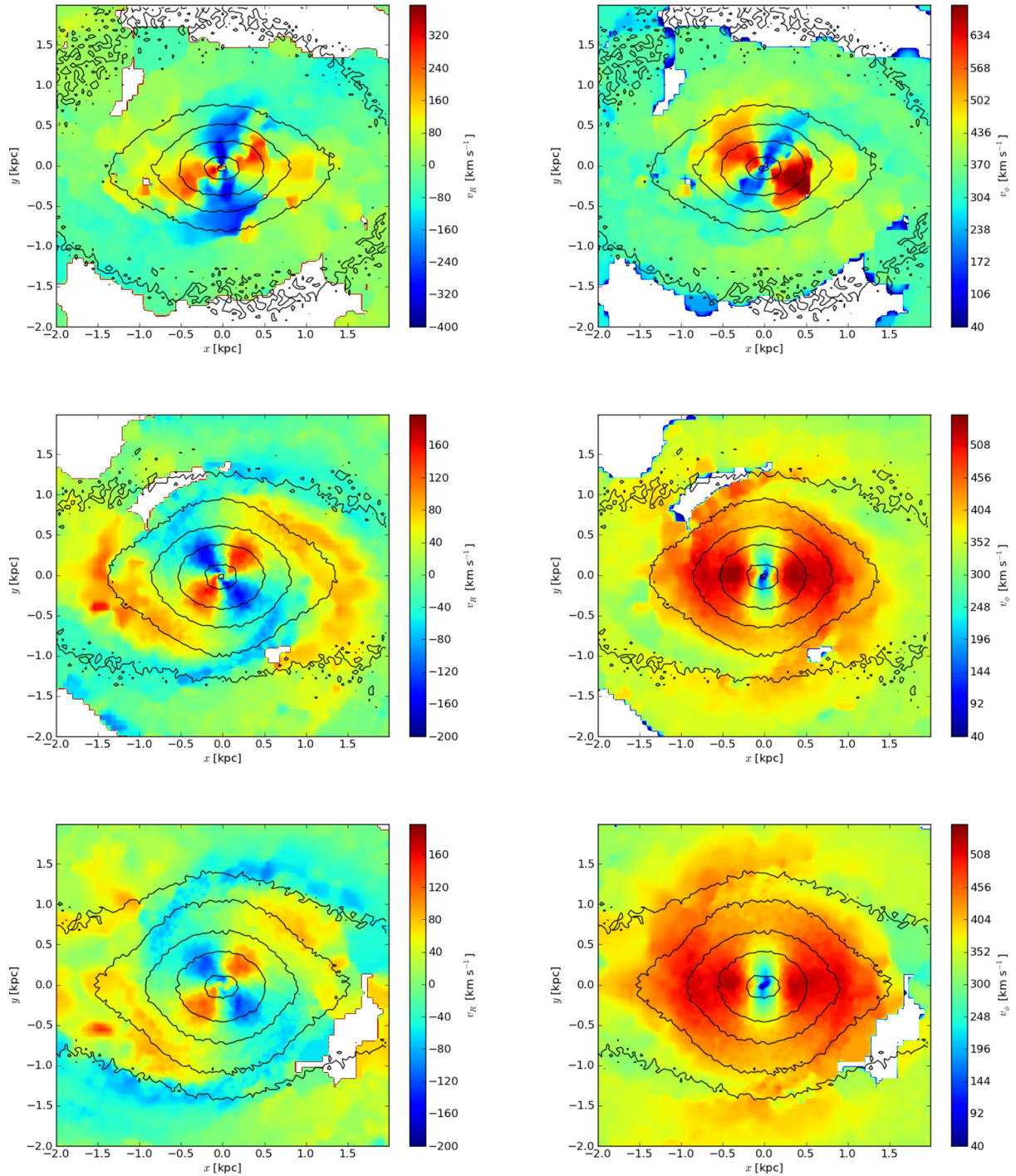


**Figure 13.** The cool gas kinematics. The left-hand column shows  $v_R$  while the right-hand column shows  $v_\phi$ . Top is at 6 Gyr, middle is at 8 Gyr and bottom is at 10 Gyr. The stellar surface density is indicated by the contours. Note the change in scale between the 6 Gyr frames and the rest.

then the ND size is 0.14. In comparison, the simulation has a ND of size 0.34 relative to the radius of peak ellipticity (0.3 relative to the radius at which the bar phase deviates from a constant by more than  $10^\circ$ ). Thus the ND in the model is about twice as large as the one in NGC 4371.

### 6.1.2 Comparison to NGC 3945

NGC 3945 is a double-barred S0 galaxy at a distance of approximately 19.8 Mpc (based on the Virgocentric-corrected HyperLeda

redshift and a Hubble constant of  $72 \text{ km s}^{-1} \text{ kpc}^{-1}$ ). Its orientation is very similar to that of NGC 4371 (bar  $\Delta\text{PA} = 88^\circ$ , inclination =  $55^\circ$ ). Unlike NGC 4371, NGC 3945 also has a small nuclear bar (Erwin et al. 2003), which our model does not.

The primary bar in NGC 3945 is aligned almost along the minor axis of the projected disc; the outer isophotes have an ellipticity of  $\approx 0.41$ , indicating an inclination of  $i \approx 55^\circ$ . The plotted isophotes (upper right-hand panel of Fig. 16) are derived from an *r*-band image from the INT/WFC (Erwin et al. 2008), while the ellipse fits are based on this image and an *HST*/Wide Field and

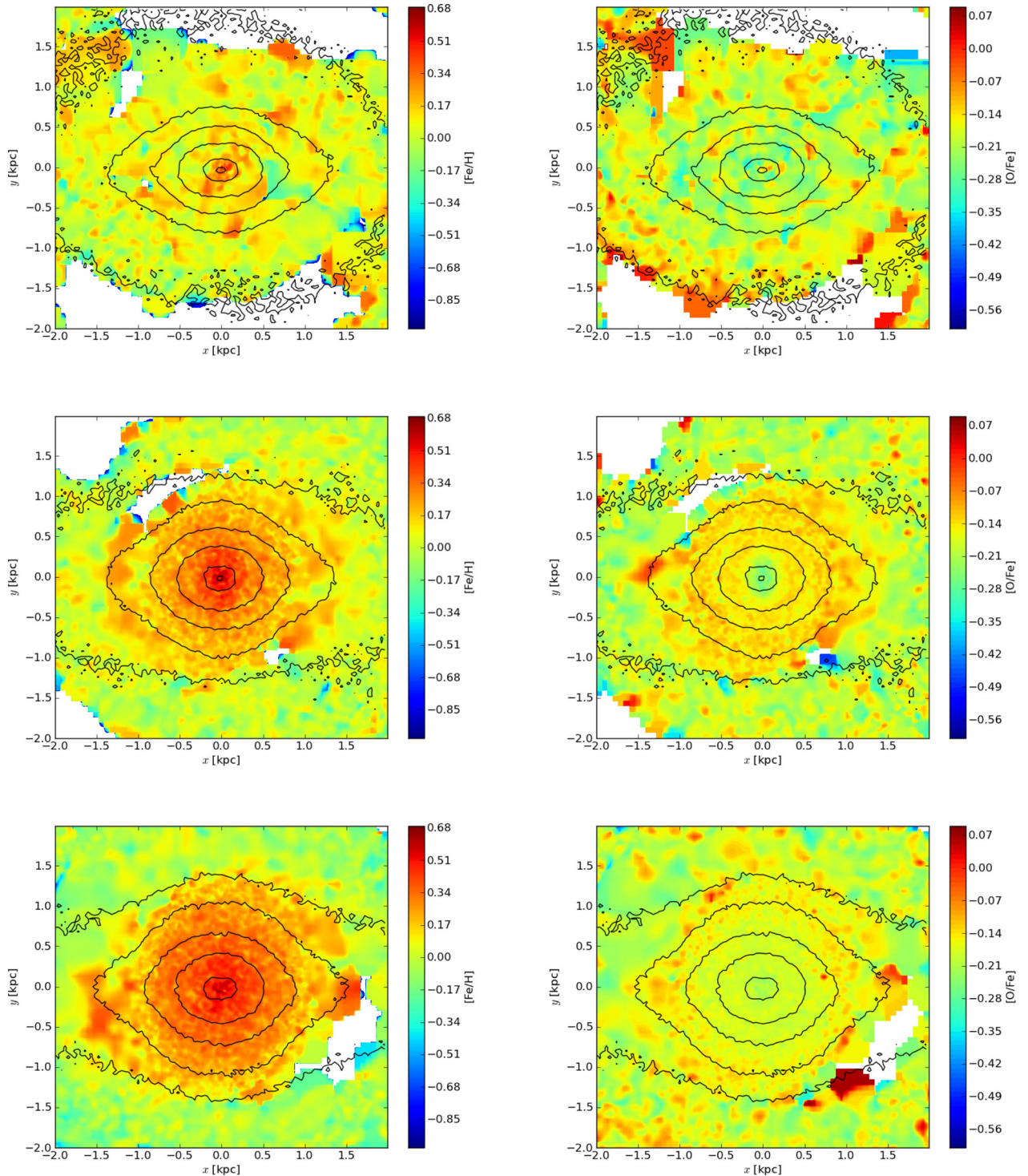


**Figure 14.** The cool gas chemistry. The left-hand column shows  $[\text{Fe}/\text{H}]$  and the right-hand column shows  $[\text{O}/\text{Fe}]$ . The top row is at 6 Gyr, the middle row at 8 Gyr and the bottom row at 10 Gyr. The stellar surface density is indicated by the contours.

Planetary Camera 2 (WFPC2) *F814W* image (PI: Carollo, proposal ID 6633).

Because the orientation is almost identical to that of NGC 4371, the appearance of the projected simulation and the ellipse fits are very similar to the previous case, and we refer the reader to Section 6.1.1 for more details. As in the case of NGC 4371, the resemblance between the simulation and the real galaxy is rather good for

the outer isophotes, including a distinct ellipticity peak corresponding to the outer ring (much more prominent in this galaxy than in NGC 4371). There is an extra ellipticity peak in NGC 3945 at a semimajor axis of  $a \sim 5.5$  kpc, in between the bar and the outer ring; this is due to the outer edge of the lens surrounding the bar.

Interior to the bar (which has its maximum ellipticity at  $a \sim 3.1$  kpc, corresponding to a deprojected semimajor axis of



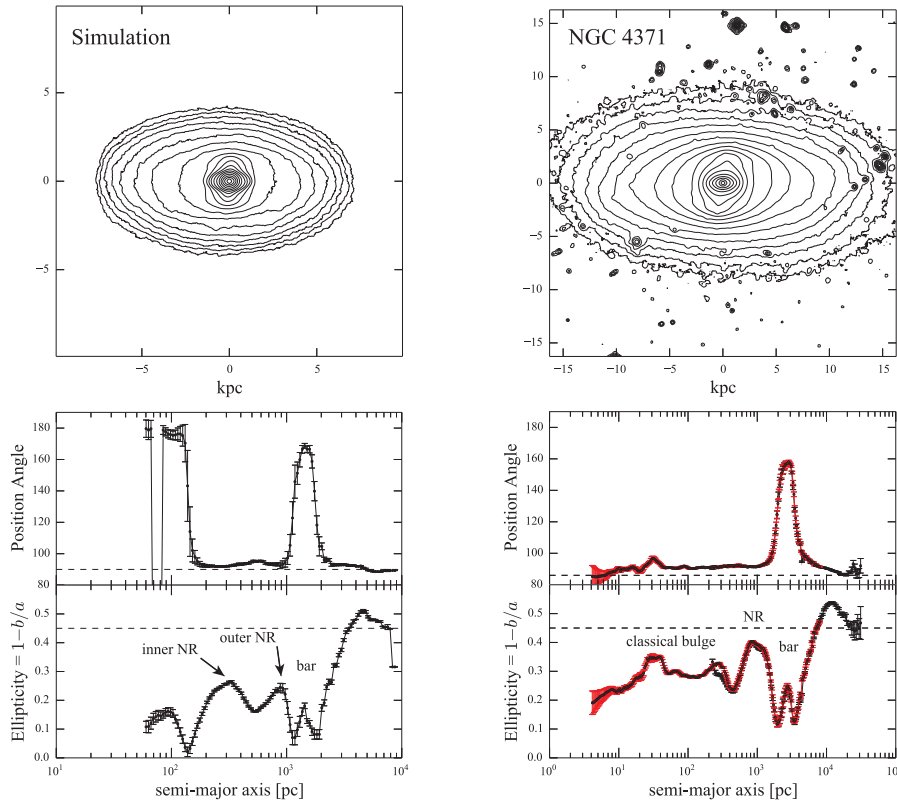


**Figure 15.** Comparison of simulation with S0 galaxy NGC 4371. Top panels: log-scaled isodensity contours (left) and  $r$ -band isophotes (right), median-smoothed, scaled so that the bar is approximately the same apparent size. The simulation (left) is oriented to match NGC 4371 (bar at deprojected  $\Delta\text{PA} = 85^\circ$  relative to the major axis, galaxy inclination =  $58^\circ$ ); both have been rotated to make the outer disc major axis horizontal in the panels. Bottom panels: ellipse fits, plotted on a logarithmic semimajor axis scale; the NGC 4371 plots (right) combine ellipse fits to the INT/WFC  $r$ -band image from the top right-hand panel (black) and an *HST* ACS  $F850LP$  image (red). In the simulation plot (left-hand panel), the PA is plotted so that the major axis is at  $\approx 90^\circ$ ; the PA for NGC 4371 is the observed value, measured CCW from north. Dashed lines indicate estimated outer disc PA and ellipticity. Labels indicate features corresponding to the inner and outer nuclear rings and the bar in the simulation ('inner NR', 'outer NR', 'bar'), along with the classical bulge, nuclear ring and bar in NGC 4371 ('classical bulge', 'NR', 'bar').

5.3 kpc), NGC 3945 shows a strong ellipticity peak ( $a \sim 1$  kpc) due to its ND.<sup>2</sup> As shown by Erwin & Sparke (1999), there is a stellar nuclear ring within this disc, which produces the slight shoulder in the ellipticity profile at  $a \sim 600$  pc. Further inside is a secondary bar oriented almost parallel to the primary bar and thus close to the galaxy minor axis; the projection of this produces the ellipticity *minimum* at  $a \sim 250$  pc; a small classical-bulge component dominates the isophotes at  $a \lesssim 100$  pc (Erwin et al. 2003, 2014).

Erwin et al. (2014) estimate a ND mass of  $2.7 \times 10^{10} M_\odot$  for NGC 3945, or 36 per cent of the total stellar mass, larger than the 29 per cent we estimate for the model at 10 Gyr using the same method. Erwin et al. (2014) measure an exponential scale length of the ND of 494 pc. Their estimate of the ND size in terms of the deprojected radius of peak ellipticity of the bar is  $\simeq 0.15$ , comparable to NGC 4371 and smaller than in the simulation.

### 6.1.3 Comparison to NGC 3368

NGC 3368 is a double-barred Sab galaxy in the Leo group with a Cepheid distance of 10.05 Mpc (Freedman et al. 2001). Although it is only slightly less inclined than NGC 3945 ( $i \approx 50^\circ$ , for an

outer disc ellipticity of 0.34), its bar is at a more intermediate PA (bar  $\Delta\text{PA} = 67^\circ$ ). The plotted isophotes (upper right-hand panel of Fig. 17) are based on a *Spitzer* Infrared Array Camera 1 (IRAC1) image from the Local Volume Legacy (Dale et al. 2009); the ellipse fits are based on this image, the  $K$ -band image of Knapen et al. (2003) and an *HST*/Near Infrared Camera and Multi-Object Spectrometer (NICMOS)  $F160W$  image (Martini et al. 2003).

Superficially, the trend in ellipticity interior to the primary bar in NGC 3368 is similar to that in the simulation: a weak peak or shoulder at  $a \sim 1$  kpc plus a more distinct peak at a smaller semimajor axis ( $a \sim 150$  pc in NGC 3368 and  $a \sim 300$  pc in the simulation). However, the underlying structures are different. As noted above, the two peaks in the simulation's ellipticity profile are due to the outer and inner nuclear rings of the ND. The outer peak/shoulder in NGC 3368's ellipticity profile, on the other hand, is due to the projected B/P structure of the bar (see Erwin & Debattista 2013), and the inner peak is due to the secondary bar. The ND in NGC 3368 shows up in the ellipticity profile as a slight bump in ellipticity at  $a \sim 400$ –500 pc, and in the PA profile as the local maximum in the same semimajor axis range.<sup>3</sup> NGC 3368 has a much more prominent B/P structure and a significantly smaller ND (with an embedded secondary bar) than is the case for the simulation.

<sup>2</sup> This is the same structure which was termed an 'inner disc' by Erwin et al. (2003) and Erwin (2004).

<sup>3</sup> Note that the 'inner disc' identified by Erwin (2004) is actually the projected B/P structure.



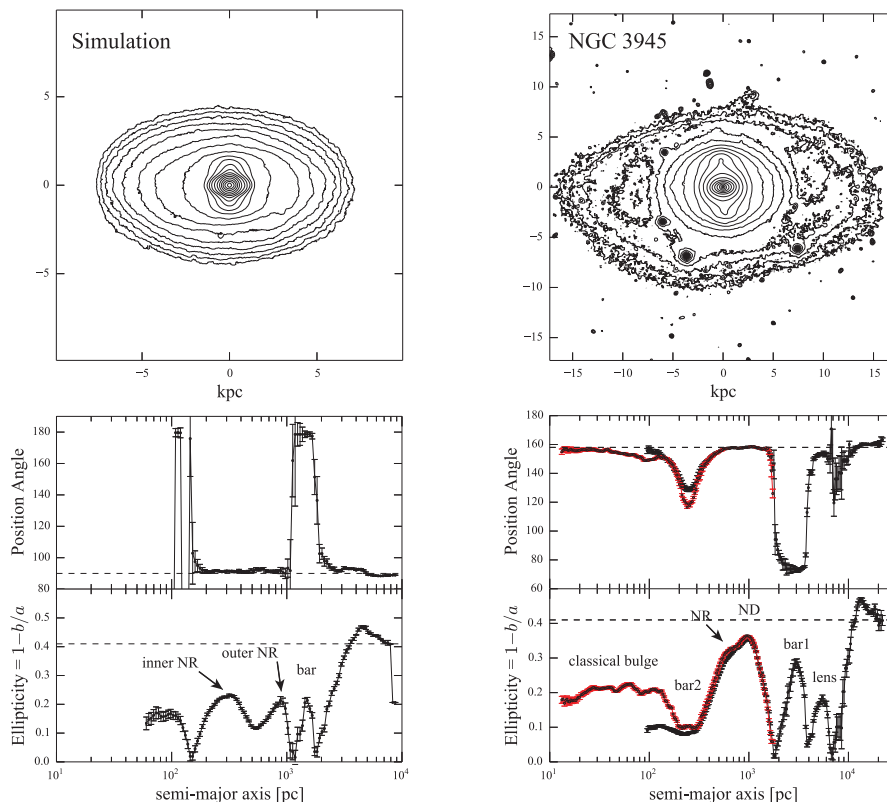


**Figure 16.** As for Fig. 15, but now comparing the simulation with the double-barred S0 galaxy NGC 3945. Simulation and galaxy orientation are: primary bar at  $\Delta PA = 88^\circ$ ; inclination =  $55^\circ$ . The ellipse fit plots use data from an INT/WFC  $r$ -band image (black) and an *HST* WFPC2  $F814W$  image (red). In the lower right-hand panel, labels indicate features corresponding to the compact classical bulge, the secondary bar, the nuclear ring, the ND and the primary bar in NGC 3945 (‘classical bulge’, ‘bar2’, ‘NR’, ‘ND’, ‘bar1’).

Erwin et al. (2014) estimates a ND mass of  $7.1 \times 10^9 M_\odot$  for NGC 3368, or 11 per cent of the total stellar mass, about a factor of 2 lower than in the model at 10 Gyr. The size of the ND is 0.12 relative to the deprojected radius of maximum ellipticity. As with NGC 4371 and NGC 3945, the ND in the model is about twice as large as in this galaxy. The scale length of the ND in NGC 3368 is 156 pc.

## 6.2 Kinematic comparisons

Integral field kinematic data from the ATLAS<sup>3D</sup> (Cappellari et al. 2011) are available for NGC 4371 and NGC 3945 (Krajnović et al. 2011). Fig. 18 shows kinematic maps ( $v_{\text{los}}$ ,  $\sigma_{\text{los}}$ ,  $h_3$ ,  $h_4$ ) for the model at 10 Gyr projected to the same orientation as NGC 3945.  $v_{\text{los}}$  has a peak on the major axis of the ND (i.e. roughly the inclination axis).  $v_{\text{los}}$  and  $h_3$  are anticorrelated in the simulation, as in the observational data, providing further evidence for the rapidly rotating ND. Within  $\sim 100$  pc (which is not resolved in the model),  $\sigma_{\text{los}}$  is peaked but is relatively flat beyond on the major axis of the ND, in agreement with the observations. On the other hand,  $h_4$  has a distinct minimum of  $\sim -0.2$  while the observational data have  $h_4 \sim 0.2$ . The face-on map of Fig. 9, however, has a quite strong maximum on the major axis of the ND, suggesting that the minimum in  $h_4$  at the orientation of NGC 3945 is too sensitive to orientation to be a useful diagnostic. Indeed we find that a negative  $h_4$  in the model requires an inclination  $< 25^\circ$ .

Following the analysis of Erwin et al. (2014) Fig. 19 plots the ratio  $v_{\text{dp}}/\sigma$ , where  $v_{\text{dp}}$  is the deprojected velocity along the disc

major axis, and  $\sigma$  is the line-of-sight velocity dispersion. The observational data are from Fabricius et al. (2012) (NGC 3945) and Erwin et al. (2014) (NGC 4371). Data for NGC 3945 are shown as (red) circles, for NGC 4371 as (black) triangles and for the model at 10 Gyr as (blue) stars. The model has been projected to bar PA =  $88^\circ$  and inclination =  $55^\circ$ , to match NGC 3945. In the left-hand panel we normalize the radius by  $R_\epsilon$ , the deprojected radius at which the bar ellipticity peaks (56 arcsec = 5.4 kpc for NGC 3945, 64 arcsec = 5.2 kpc for NGC 4371 and 2.65 kpc for the model). The right-hand panel instead normalizes the radius by  $R_{\text{ND}}$ , the radius of the peak ellipticity in the ND region. In the left-hand panel, the  $v_{\text{dp}}/\sigma$  rises more slowly in the model than in the observations, consistent with the ND being larger, relative to the bar, than in the observations, but reaches values intermediate between NGC 3945 and NGC 4371. In all cases,  $v_{\text{dp}}/\sigma > 1$  by the edge of the ND (right-hand panel). The dashed vertical lines indicate the radius of peak ellipticity in the ND region. In the observations  $v_{\text{dp}}/\sigma$  then declines again, but no such drop is present in the model although the slope of  $v_{\text{dp}}/\sigma$  is considerably shallower. Given that the observational data are for lenticular galaxies, while our model is star forming, this difference between the observations and the model can be understood as arising from discs in NGC 3945 and NGC 4371 that become relatively hotter beyond the ND than in the model.

## 7 DISCUSSION

We have presented a simulation of an  $L_*$  barred spiral galaxy with a prominent ND. The ND is elliptical and perpendicular to the

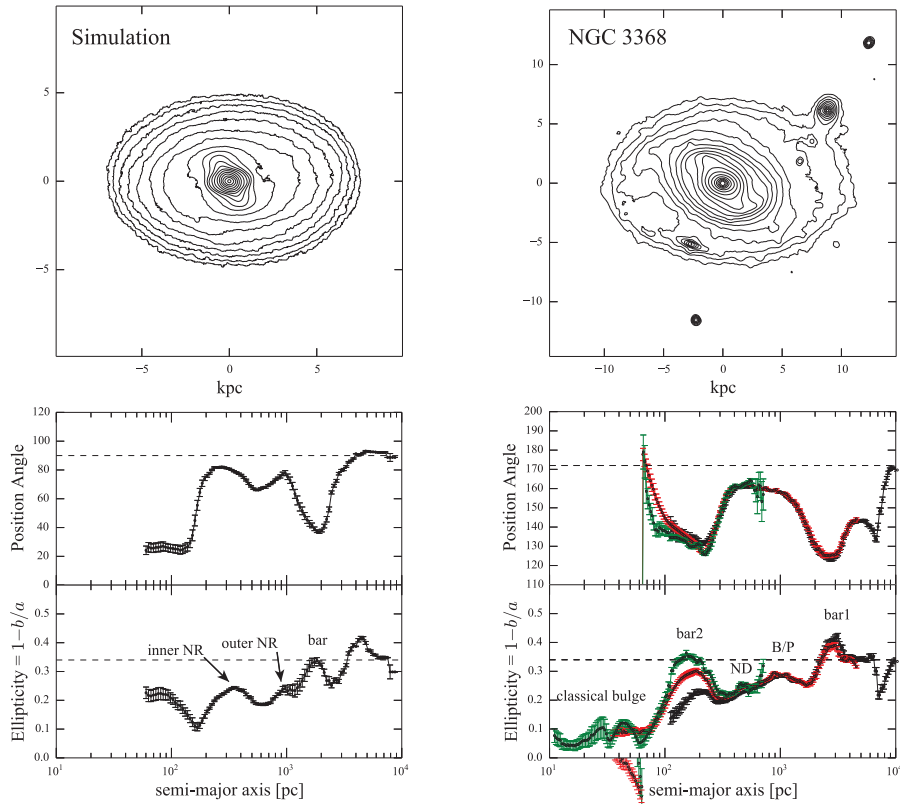


**Figure 17.** As for Fig. 15, but now comparing the simulation with the double-barred Sab galaxy NGC 3368. Simulation and galaxy orientation are: primary bar at  $\Delta\text{PA} = 67^\circ$ ; inclination =  $50^\circ$ . The ellipse fit plots use data from a *Spitzer* IRAC1 image (black), the *K*-band image of Knapen et al. (2003) (red) and an *HST* NICMOS2 *F160W* image (green). In the lower right-hand panel, labels indicate features corresponding to the compact classical bulge, the secondary bar, the ND, the projected B/P structure of the primary bar and the primary bar itself in NGC 3368 (‘classical bulge’, ‘bar2’, ‘ND’, ‘B/P’, ‘bar1’).

bar. The disc develops after 6 Gyr, during an episode when the bar strengthens; the ND therefore contains younger stars.

The stellar kinematics are affected by the presence of the ND, particularly on the major axis of the ND, i.e. the minor axis of the bar. In this area, the mass-weighted mean tangential velocities are dominated by the ND rotation in an elliptical disc. The growth of the ND forces the peak inflow and outflow radial velocities to lie closer to the bar major axis. These kinematics can be understood as the superposition of the motions of (older) stars streaming along the bar’s major axis, and of the (younger) stars in a ND elongated perpendicular to the bar. It is also on the minor axis of the bar that the ND most affects the mass-weighted velocity dispersions, both radially and vertically. The ND also alters the mass-weighted  $h_4$  kinematic moment of the vertical motion along the major axis of the ND, producing large peaks, indicative of a peaked line-of-sight velocity distribution.

The gas kinematics within the central 1 kpc at 6 Gyr show inflows and outflows. At the location of the inflows the density is in general higher, resulting in a net accumulation of gas at the centre. Once the ND forms, there is a high gas density throughout the ND region. Two spiral arms of gas connect to the major apices of the disc where radial inward velocities trace dense gas in the spiral arms showing continuing feeding of the gas to the disc. By 8 Gyr the gas has settled into the ND but shows continuing inflow along spiral arms which connect to the gas at the apices of the ND.

The stellar chemistry also shows evidence of the continuing processes feeding star formation. There is increasing  $[\text{Fe}/\text{H}]$  in the disc from 6 to 8 Gyr with  $[\text{O}/\text{Fe}]$  declining. The ND can be iden-

tified clearly in maps of  $[\text{Fe}/\text{H}]$ , but the  $[\text{O}/\text{Fe}]$  maps contain no distinct signature of the ND. Gas chemistry also shows a strong increase in  $[\text{Fe}/\text{H}]$  after 8 Gyr, reflecting the enhanced star formation there, even as low-metallicity gas feeds in from outside the central kiloparsec.

We compare the morphological and kinematic properties of the model with data for the early-type galaxies NGC 4371, NGC 3945 and NGC 3368. We find broad similarities. The main difference is in the size of the ND relative to the bar, which in the model is roughly twice as large as in the observations. This may possibly be due to the absence of gas in the early-type galaxies we have compared. In order to check this, we re-ran part of our simulation from 7 Gyr with star formation turned off. By 9 Gyr the resulting ND is smaller relative to the bar. Using the radius at which the bar phase deviates from a constant by more than  $10^\circ$  to measure the bar length at 9 Gyr, the ND is 0.32 times the bar length with star formation and 0.24 without, a 25 per cent difference. When gas is absent, the bar can grow more rapidly while the ND remains largely unchanged. While our ND is larger than in those galaxies, its kinematics are generally similar. This includes an anticorrelation between  $h_3$  and  $v_{\text{los}}$  along the ND, a relatively flat  $\sigma_{\text{los}}$  in the ND, and a  $v_{\text{dp}}/\sigma$  profile that reaches values intermediate to those observed by the end of the ND. This implies that the NDs in these galaxies grew via gas inflows as in the simulation. Thus the simulation clearly demonstrates that gas inflows play an important role in the continued assembly of structure at the nuclei of galaxies. Although gas-rich galaxy mergers have been suggested as a mechanism for driving gas to the centres to fuel the formation of NDs (Mayer et al. 2008; Chapon et al. 2013) our

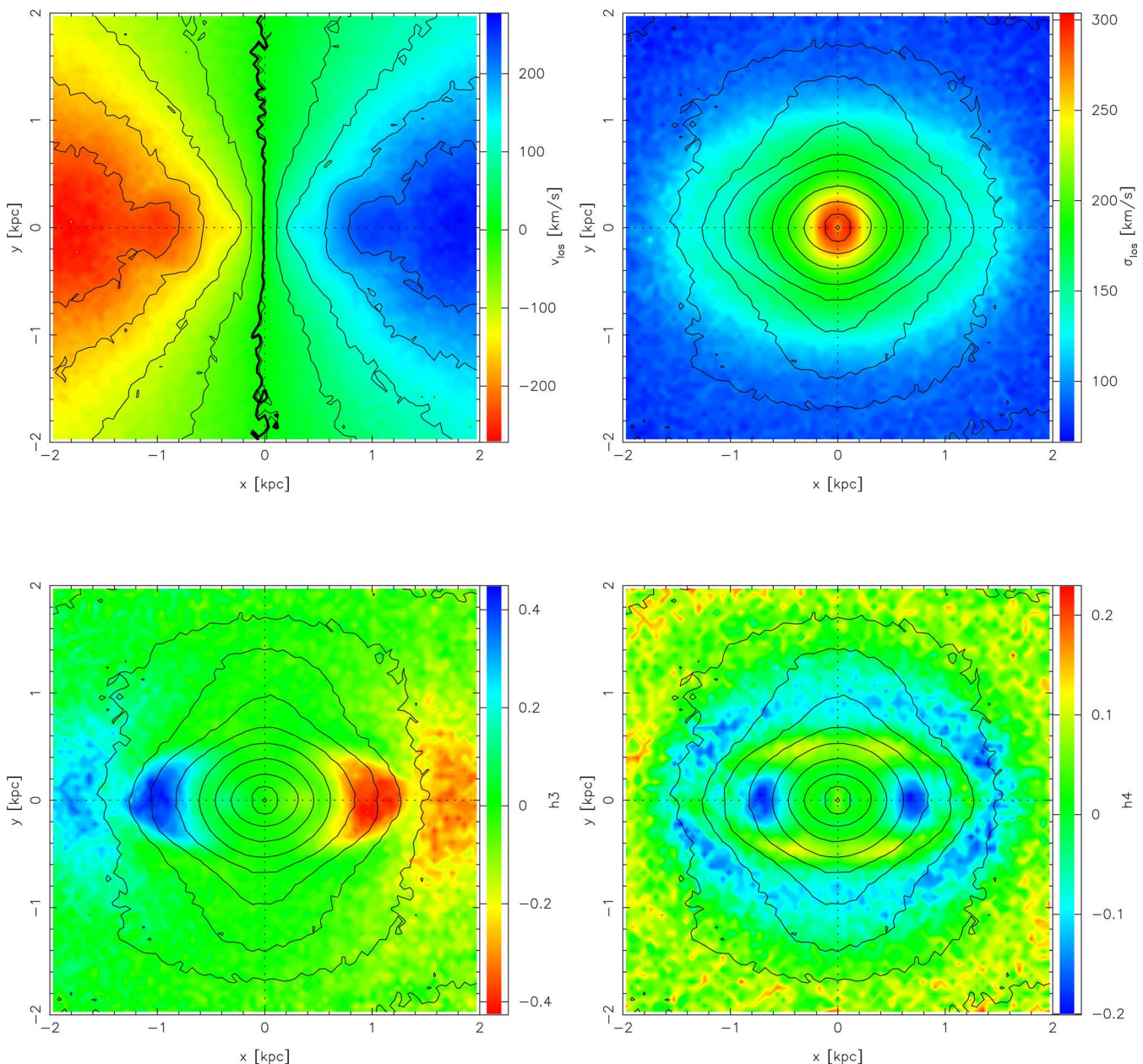


**Figure 18.** Line-of-sight kinematic maps for the model at 10 Gyr projected to the orientation of NGC 3945 (bar PA =  $88^\circ$ , here measured from the  $x$ -axis, inclination =  $55^\circ$ ). Top left is  $v_{\text{los}}$ , top right is  $\sigma_{\text{los}}$ , bottom left is  $h_3$ , bottom right is  $h_4$ . The  $v_{\text{los}}$  map shows contours of isovelocity, with the  $v_{\text{los}} = 0$  shown in bold, while the remaining maps show contours of surface density. The bar is nearly vertical in this image, while the ND is almost horizontal.

model demonstrates that they can also form due to purely internal evolutionary processes.

### 7.1 Implications for nuclear star clusters

The morphology of our model is able to feed gas to the central 100 pc of a galaxy and fuel ongoing star formation there. Seth et al. (2006) find that nuclear star clusters are typically elongated in the plane of the galaxy disc and are compound structures having a younger thin disc embedded in an older spheroidal component. Integral Field Spectroscopy shows rotation in the same sense as the galaxy (Seth et al. 2008). Our model shows that the creation of such discs is a natural consequence of secular evolution in a galaxy. Gas falls in to

the nuclear regions due to dynamical evolution of the bar which in turn causes increased star formation.

Recent observations of the Milky Way’s nuclear star cluster show that it is significantly flattened in the same direction as the Galactic disc (Schodel et al. 2014), supporting the idea that it has formed via gas inflows and in situ star formation. Our model supports the view that gas can be fed to such small radii to fuel ongoing episodic star formation (Pfuhl et al. 2011). Though it is clear that the merger of globular clusters at the centre is a plausible process for growing nuclear star clusters (Tremaine, Ostriker & Spitzer 1975; Capuzzo-Dolcetta 1993; Capuzzo-Dolcetta & Miocchi 2008; Antonini et al. 2012; Antonini 2013; Gnedin, Ostriker & Tremaine 2014), helping explain some kinematic anomalies (Hartmann et al.



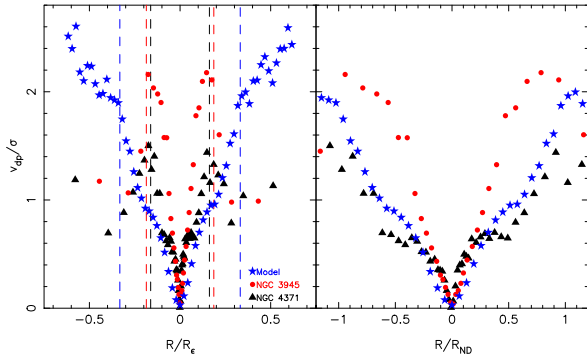


**Figure 19.**  $v_{dp}/\sigma$  along the major axis for NGC 3945 (red circles), NGC 4371 (black triangles) and the model at 10 Gyr (blue stars). Left-hand panel: radii normalized by the radius of the peak ellipticity within the bar,  $R_e$ . The vertical dashed lines correspond to the radii of the peak ellipticities of the nuclear discs,  $R_{ND}$ . Right-hand panel: same as left-hand panel but with radii normalized by  $R_{ND}$ . Real galaxy data from Erwin et al. (2014) (NGC 4371) and Fabricius et al. (2012) (NGC 3945).

2011; De Lorenzi et al. 2013), it is likely that in situ star formation plays a more significant role.

## ACKNOWLEDGEMENTS

We would like to thank the referee Ronald Buta for his valuable comments. DRC and VPD are supported by STFC Consolidated grant # ST/J001341/1. RR is partially supported by Marie Curie Career Integration Grant. The simulation used in this study was run at the High Performance Computer Facility of the University of Central Lancashire. We made use of `PYNBODY` (<https://github.com/pynbody/pynbody>) in our analysis for this paper.

## REFERENCES

Agarwal M., Milosavljević M., 2011, *ApJ*, 729, 35  
 Antonini F., 2013, *ApJ*, 763, 62  
 Antonini F., Capuzzo-Dolcetta R., Mastrobuono-Battisti A., Merritt D., 2012, *ApJ*, 750, 111  
 Balcells M., Graham A. W., Domínguez-Palmero L., Peletier R. F., 2003, *ApJ*, 582, L79  
 Balcells M., Graham A. W., Peletier R. F., 2007, *ApJ*, 665, 1084  
 Bekki K., 2007, *Publ. Astron. Soc. Aust.*, 24, 77  
 Bensby T. et al., 2011, *A&A*, 533, A134  
 Bensby T. et al., 2013, *A&A*, 549, A147  
 Bertola F., Corsini E. M., Vega Beltrán J. C., Pizzella A., Sarzi M., Cappellari M., Funes J. G., 1999, *ApJ*, 519, L127  
 Blakeslee J. P. et al., 2009, *ApJ*, 694, 556  
 Cappellari M. et al., 2011, *MNRAS*, 413, 813  
 Capuzzo-Dolcetta R., 1993, *ApJ*, 415, 616  
 Capuzzo-Dolcetta R., Miocchi P., 2008, *MNRAS*, 388, L69  
 Chang C.-K., Ko C.-M., Peng T.-H., 2011, *ApJ*, 740, 34  
 Chapon D., Mayer L., Teyssier R., 2013, *MNRAS*, 429, 3114  
 Comerón S., Knapen J. H., Beckman J. E., 2008, *A&A*, 485, 695  
 Comerón S., Knapen J. H., Beckman J. E., Laurikainen E., Salo H., Martínez-Valpuesta I., Buta R. J., 2010, *MNRAS*, 402, 2462  
 Corsini E. M. et al., 1999, *A&A*, 342, 671  
 Corsini E. M., Méndez-Abreu J., Pastorello N., Dalla Bontà E., Morelli L., Beifiori A., Pizzella A., Bertola F., 2012, *MNRAS*, 423, L79  
 Côté P. et al., 2004, *ApJS*, 153, 223  
 Dale D. A. et al., 2009, *ApJ*, 703, 517  
 Debattista V. P., Sellwood J. A., 2000, *ApJ*, 543, 704  
 Debattista V. P., Carollo C. M., Mayer L., Moore B., 2005, *ApJ*, 628, 678

De Lorenzi F., Hartmann M., Debattista V. P., Seth A. C., Gerhard O., 2013, *MNRAS*, 429, 2974  
 de Zeeuw P. T. et al., 2002, *MNRAS*, 329, 513  
 Dumas G., Mundell C. G., Emsellem E., Nagar N. M., 2007, *MNRAS*, 379, 1249  
 Emsellem E., Greusard D., Combes F., Friedli D., Leon S., Pécontal E., Wozniak H., 2001, *A&A*, 368, 52  
 Emsellem E. et al., 2004, *MNRAS*, 352, 721  
 Erwin P., 2004, *A&A*, 415, 941  
 Erwin P., Debattista V. P., 2013, *MNRAS*, 431, 3060  
 Erwin P., Sparke L. S., 1999, *ApJ*, 521, L37  
 Erwin P., Vega Beltrán J. C., Beckman J. E., 2001, in Knapen J. H., Beckman J. E., Shlosman I., Mahoney T. J., eds, *ASP Conf. Ser. Vol. 249, The Central Kiloparsec of Starbursts and AGN: The La Palma Connection*. Astron. Soc. Pac., San Francisco, p. 171  
 Erwin P., Vega Beltrán J. C., Graham A. W., Beckman J. E., 2003, *ApJ*, 597, 929  
 Erwin P., Pohlen M., Beckman J. E., 2008, *AJ*, 135, 20  
 Erwin P. et al., 2014, *MNRAS*, submitted  
 Fabricius M. H., Saglia R. P., Fisher D. B., Drory N., Bender R., Hopp U., 2012, *ApJ*, 754, 67  
 Falcón-Barroso J. et al., 2004, *MNRAS*, 350, 35  
 Freedman W. L. et al., 2001, *ApJ*, 553, 47  
 García-Burillo S., Combes F., 2012, *J. Phys. Conf. Ser.*, 372, 012050  
 Gardner E., Debattista V. P., Robin A. C., Vásquez S., Zoccali M., 2014, *MNRAS*, 438, 3275  
 Gnedin O. Y., Ostriker J. P., Tremaine S., 2014, *ApJ*, 785, 71  
 Governato F. et al., 2010, *Nature*, 463, 203  
 Hao L., Jogee S., Barazza F. D., Marinova I., Shen J., 2009, in Jogee S., Marinova I., Hao L., Blanc G. A., eds, *ASP Conf. Ser. Vol. 419, Galaxy Evolution: Emerging Insights and Future Challenges*. Astron. Soc. Pac., San Francisco, p. 402  
 Hartmann M., Debattista V. P., Seth A., Cappellari M., Quinn T. R., 2011, *MNRAS*, 418, 2697  
 Hicks E. K. S., Davies R. I., Maciejewski W., Emsellem E., Malkan M. A., Dumas G., Müller-Sánchez F., Rivers A., 2013, *ApJ*, 768, 107  
 Knapen J. H., de Jong R. S., Stedman S., Bramich D. M., 2003, *MNRAS*, 344, 527  
 Kormendy J., Gebhardt K., 2001, in Wheeler J. C., Martel H., eds, *AIP Conf. Ser. Vol. 586, Relativistic Astrophysics: 20th Texas Symposium*. Am. Inst. Phys., New York, p. 363  
 Kormendy J., Kennicutt R. C., Jr, 2004, *ARA&A*, 42, 603  
 Kormendy J., Dressler A., Byun Y. I., Faber S. M., Grillmair C., Lauer T. R., Richstone D., Tremaine S., 1994, in Meylan G., Prugniel P., eds, *ESO Conference and Workshop Proceedings, Vol. 49, Dwarf Galaxies*. ESO, Garching, p. 147  
 Kormendy J., Gebhardt K., Fisher D. B., Drory N., Macchetto F. D., Sparks W. B., 2005, *AJ*, 129, 2636  
 Krajnović D., Jaffe W., 2004, *A&A*, 428, 877  
 Krajnović D. et al., 2008, *MNRAS*, 390, 93  
 Krajnović D. et al., 2011, *MNRAS*, 414, 2923  
 Lambas D. G., Maddox S. J., Loveday J., 1992, *MNRAS*, 258, 404  
 Ledo H. R., Sarzi M., Dotti M., Khochfar S., Morelli L., 2010, *MNRAS*, 407, 969  
 Loebman S. R., Roškar R., Debattista V. P., Ivezić Ž., Quinn T. R., Wadsley J., 2011, *ApJ*, 737, 8  
 Lyubenova M. et al., 2013, *MNRAS*, 431, 3364  
 McDermid R. M. et al., 2006, *MNRAS*, 373, 906  
 McMillan P. J., 2011, *MNRAS*, 414, 2446  
 Martini P., Regan M. W., Mulchaey J. S., Pogge R. W., 2003, *ApJS*, 146, 353  
 Mayer L., Kazantzidis S., Escala A., 2008, *Mem. Soc. Astron. Ital.*, 79, 1284  
 Mayer L., Kazantzidis S., Escala A., Callegari S., 2010, *Nature*, 466, 1082  
 Medling A. M. et al., 2014, *ApJ*, 784, 70  
 Méndez-Abreu J., Debattista V. P., Corsini E. M., Aguerri J., 2014, preprint ([arXiv:1405.0001](https://arxiv.org/abs/1405.0001))  
 Méndez-Abreu J., Corsini E. M., Debattista V. P., De Rijcke S., Aguerri J. A. L., Pizzella A., 2008, *ApJ*, 679, L73

- Miller G. E., Scalo J. M., 1979, *ApJS*, 41, 513
- Milosavljević M., 2004, *ApJ*, 605, L13
- Morelli L. et al., 2004, *MNRAS*, 354, 753
- Morelli L., Cesetti M., Corsini E. M., Pizzella A., Dalla Bontà E., Sarzi M., Bertola F., 2010, *A&A*, 518, A32
- Ness M., Debattista V. P., Bensby T., Feltzing S., Roskar R., Cole D. R., Johnson J. A., Freeman K., 2014, *ApJ*, 787, L19
- Nowak N., Thomas J., Erwin P., Saglia R. P., Bender R., Davies R. I., 2010, *MNRAS*, 403, 646
- Ojha D. K., 2001, *MNRAS*, 322, 426
- Padilla N. D., Strauss M. A., 2008, *MNRAS*, 388, 1321
- Pfuhl O. et al., 2011, *ApJ*, 741, 108
- Pizzella A., Corsini E. M., Morelli L., Sarzi M., Scarlata C., Stiavelli M., Bertola F., 2002, *ApJ*, 573, 131
- Portinari E., Corsini E. M., Morelli L., Hartmann M., Dalla Bontà E., Debattista V. P., Pizzella A., 2013, *MNRAS*, 433, 434
- Ravindranath S., Ho L. C., Peng C. Y., Filippenko A. V., Sargent W. L. W., 2001, *AJ*, 122, 653
- Rodríguez S., Padilla N. D., 2013, *MNRAS*, 434, 2153
- Roškar R., Debattista V. P., Stinson G. S., Quinn T. R., Kaufmann T., Wadsley J., 2008, *ApJ*, 675, L65
- Roškar R., Debattista V. P., Quinn T. R., Wadsley J., 2012, *MNRAS*, 426, 2089
- Rossa J., van der Marel R. P., Böker T., Gerssen J., Ho L. C., Rix H.-W., Shields J. C., Walcher C.-J., 2006, *AJ*, 132, 1074
- Sakamoto K., Okumura S. K., Ishizuki S., Scoville N. Z., 1999, *ApJ*, 525, 691
- Schinnerer E., Böker T., Meier D. S., 2003, *ApJ*, 591, L115
- Schodel R., Feldmeier A., Kunneriath D., Stolovy S., Neumayer N., Amaro-Seoane P., Nishiyama S., 2014, *A&A*, 566, A47
- Scorza C., van den Bosch F. C., 1998, *MNRAS*, 300, 469
- Seifert W., Scorza C., 1996, *A&A*, 310, 75
- Sellwood J. A., Wilkinson A., 1993, *Rep. Progress Phys.*, 56, 173
- Seth A. C., Dalcanton J. J., Hodge P. W., Debattista V. P., 2006, *AJ*, 132, 2539
- Seth A. C., Blum R. D., Bastian N., Caldwell N., Debattista V. P., 2008, *ApJ*, 687, 997
- Seth A. C. et al., 2010, *ApJ*, 714, 713
- Sheth K., Vogel S. N., Regan M. W., Thornley M. D., Teuben P. J., 2005, *ApJ*, 632, 217
- Shlosman I., Frank J., Begelman M. C., 1989, *Nature*, 338, 45
- Skokos C., Patsis P. A., Athanassoula E., 2002, *MNRAS*, 333, 847
- Stinson G., Seth A., Katz N., Wadsley J., Governato F., Quinn T., 2006, *MNRAS*, 373, 1074
- Tremaine S. D., Ostriker J. P., Spitzer L., Jr, 1975, *ApJ*, 196, 407
- Trujillo I., Erwin P., Asensio Ramos A., Graham A. W., 2004, *AJ*, 127, 1917
- Valenti E., Zoccali M., Renzini A., Brown T. M., Gonzalez O. A., Minniti D., Debattista V. P., Mayer L., 2013, *A&A*, 559, A98
- van den Bosch F. C., Jaffe W., van der Marel R. P., 1998, *MNRAS*, 293, 343
- Wadsley J. W., Stadel J., Quinn T., 2004, *New Astron.*, 9, 137
- Walcher C. J., Böker T., Charlot S., Ho L. C., Rix H.-W., Rossa J., Shields J. C., van der Marel R. P., 2006, *ApJ*, 649, 692
- Wang J. et al., 2012, *MNRAS*, 423, 3486
- Woosley S. E., Weaver T. A., 1995, *ApJS*, 101, 181
- Wozniak H., 2007, *A&A*, 465, L1
- Wozniak H., Michel-Dansac L., 2008, in Bureau M., Athanassoula E., Barbuy B., eds, *Proc. IAU Symp. 245, Formation and Evolution of Galaxy Bulges*. Cambridge Univ. Press, Cambridge, p. 143
- Wozniak H., Michel-Dansac L., 2009, *A&A*, 494, 11
- Wozniak H., Combes F., Emsellem E., Friedli D., 2003, *A&A*, 409, 469
- Zasov A. V., Moiseev A. V., 1999, in Terzian Y., Khachikian E., Weedman D., eds, *Proc. IAU Symp. 194, Active Galactic Nuclei and Related Phenomena*. Astron. Soc. Pac., San Francisco, p. 279

This paper has been typeset from a  $\text{\LaTeX}$  file prepared by the author.